University of Reading

Atmospheric adjustments to in situ cirrus formation in ice supersaturated regions

Article

Published Version

Creative Commons: Attribution 4.0 (CC-BY)

Open Access

Juvin-Quarroz, J., Borella, A., Kiepas, P., Dubos, T., Boucher, O. and Bellouin, N. ORCID: https://orcid.org/0000-0003-2109-9559 (2026) Atmospheric adjustments to in situ cirrus formation in ice supersaturated regions. Journal of Geophysical Research: Atmospheres, 131 (8). e2025JD046235. ISSN 2169-8996 doi: 10.1029/2025JD046235 Available at https://centaur.reading.ac.uk/129390/

It is advisable to refer to the publisher's version if you intend to cite from the work. See Guidance on citing.

To link to this article DOI: http://dx.doi.org/10.1029/2025JD046235

Publisher: American Geophysical Union

All outputs in CentAUR are protected by Intellectual Property Rights law, including copyright law. Copyright and IPR is retained by the creators or other copyright holders. Terms and conditions for use of this material are defined in the End User Agreement.

www.reading.ac.uk/centaur

University of Reading

CentAUR

Central Archive at the University of Reading

Reading's research outputs online

Check for updates

JGR Atmospheres

RESEARCH ARTICLE
10.1029/2025JD046235

Atmospheric Adjustments to In Situ Cirrus Formation in Ice Supersaturated Regions

Jérémie Juvin-Quarroz[1], Audran Borella[1], Patryk Kiepas[2], Thomas Dubos[2], Olivier Boucher[1], and Nicolas Bellouin[1,3]

[1]Institut Pierre–Simon Laplace, Sorbonne Université/CNRS, Paris, France, [2]Laboratoire de Météorologie Dynamique/IPSL/École Polytechnique, Institut Polytechnique de Paris, Palaiseau/CNRS, Paris, France, [3]Departement of Meteorology, University of Reading, Reading, UK

Key Points:

- Atmospheric adjustments contribute to offset the initial radiative impact of in situ cirrus cloud formation
- Cirrus formation induces a drop in relative humidity, that reduces the atmosphere's ability to sustain further ice nucleation for up to 4 days
- High-level cloud cover and radiative effects respond non-linearly to the perturbation intensity and non-uniformly across regions

Supporting Information:

Supporting Information may be found in the online version of this article.

Correspondence to:

J. Juvin-Quarroz,
jeremie.juvin-quarroz@ipsl.fr

Citation:

Juvin-Quarroz, J., Borella, A., Kiepas, P., Dubos, T., Boucher, O., & Bellouin, N. (2026). Atmospheric adjustments to in situ cirrus formation in ice supersaturated regions. *Journal of Geophysical Research: Atmospheres*, *131*, e2025JD046235. https://doi.org/10.1029/2025JD046235

Received 22 DEC 2025
Accepted 13 APR 2026

Author Contributions:

Conceptualization: Jérémie Juvin-Quarroz, Olivier Boucher, Nicolas Bellouin
Formal analysis: Jérémie Juvin-Quarroz
Funding acquisition: Nicolas Bellouin
Investigation: Jérémie Juvin-Quarroz
Methodology: Jérémie Juvin-Quarroz, Olivier Boucher, Nicolas Bellouin
Project administration: Nicolas Bellouin
Software: Jérémie Juvin-Quarroz, Audran Borella, Patryk Kiepas, Thomas Dubos
Supervision: Olivier Boucher, Nicolas Bellouin
Validation: Jérémie Juvin-Quarroz
Visualization: Jérémie Juvin-Quarroz
Writing – original draft: Jérémie Juvin-Quarroz

© 2026. The Author(s).
This is an open access article under the terms of the Creative Commons Attribution License, which permits use, distribution and reproduction in any medium, provided the original work is properly cited.

Abstract High-level ice clouds exert a net warming on the climate system because their greenhouse effect outweighs their albedo effect. Focusing on in-situ cirrus, their formation involves the conversion of upper-tropospheric water vapor into ice crystals. Anthropogenic perturbations to the upper-tropospheric water budget—such as aviation-induced cloudiness or the proposed cirrus cloud thinning concept—also trigger atmospheric adjustments that contribute to the total effective radiative forcing. This study presents an idealized climate-model pulse experiment in which water exceeding saturation within cloud-free, ice-supersaturated regions is instantaneously condensed to form cirrus clouds. In contrast to sustained perturbations, this transient modification of cirrus cloud cover enables the direct isolation and examination of atmospheric adjustments. We further introduce a novel ensemble-based framework that suppresses the statistical impact of atmospheric variability, allowing for a robust assessment of the comparatively weak atmospheric response. Cirrus cloud formation initially increases high-level cirrus cloud cover, followed by a decay as ice crystals sediment and sublimate. This process induces an immediate reduction in upper-atmospheric specific and relative humidity, with recovery occurring on substantially longer timescales. The combined cloud and humidity responses generate an initially positive radiative perturbation that transitions to a negative signal after a couple of hours. Notably, relative humidity requires up to four days to return to its equilibrium value. Adjustments in high-level cloud fraction and top-of-atmosphere longwave radiation exhibit non-linear behavior. Together, these findings elucidate how the radiative effects of cirrus clouds—whether natural or anthropogenic—are partially counteracted by atmospheric adjustments, with important implications for the climate efficacy of cirrus-related forcings.

Plain Language Summary Cirrus clouds, a type of high-level ice clouds, warm the climate overall because their heat-trapping effect is stronger than their ability to reflect sunlight. Their coverage depends on how quickly they form—mainly when vapor freezes in cold, moist air—and how fast they dissipate as ice crystals fall into warmer layers of the atmosphere or mix with surrounding air. Human activities can disrupt these processes: aviation unintentionally create cirrus through condensation trails, while some proposed methods aim to deliberately thin these clouds. However, the magnitude of these effects remains highly uncertain. This study examines an idealized case where all water vapor above saturation in cloud-free, cold regions (temperatures below −38°C) condense into ice. We determine how the upper-atmospheric water budget responds to this pulse perturbation. Initially, cirrus cloud cover increases, producing a warming effect. Over time, the clouds thin as ice crystals fall and sublimate. As a result, the radiative perturbation turns from positive to negative after a few hours. Humidity is fully restored four days after the perturbation. Furthermore some adjustment mechanisms depend on the intensity and the geographical distribution of the initial perturbation. Understanding these processes is crucial for better estimating the climate impact of cirrus cloud perturbations.

1. Introduction

Cirrus clouds are high-level clouds composed of ice crystals. Unlike low-level liquid clouds, cirrus clouds exert a positive cloud radiative effect on a global scale (Hong & Liu, 2015). Their thin, wispy structure makes them less efficient at scattering solar radiation than liquid clouds, while they produce a significant greenhouse effect due to the temperature contrast between the Upper Troposphere (UT) and the Earth's surface. Cirrus clouds thus affect the Earth's radiative budget, which itself controls the Earth's surface temperature, so changes in cirrus coverage or optical properties are relevant to Radiative Forcing (RF) of climate change and climate feedbacks (Forster

Writing – review & editing: Jérémie Juvin-Quarroz, Audran Borella, Patryk Kiepas, Olivier Boucher, Nicolas Bellouin

et al., 2021; Sherwood et al., 2015). Despite their extensive global coverage, accurately quantifying the contribution to the Earth's radiative budget of cirrus clouds remains a challenge, due to complex formation pathways, variability in microphysical properties, and uncertainties in their response to changes in environmental conditions (Ceppi et al., 2017; Chen et al., 2000; Schlimme et al., 2005; Wilson Kemsley et al., 2025; Zelinka et al., 2020, 2022).

Human activities directly affect cirrus cloudiness through changes in the UT aerosol and water budget (Kärcher, 2017). In particular, aviation is responsible for the formation of condensation trails (contrails) that may evolve into contrail cirrus. Increasing air traffic is therefore thought to have led to an increase in cirrus cloud cover (Boucher, 1999; Duda et al., 2019; Quaas et al., 2021). Furthermore, Cirrus Cloud Thinning (CCT) has been proposed as a solar radiation modification method intended to deliberately reduce high-level cloud cover and optical depth, and thereby lessen their warming contribution (Gasparini & Lohmann, 2016; Mitchell & Finnegan, 2009; Penner et al., 2015).

Perturbations to cirrus cloud cover or optical properties modify the radiative equilibrium of the climate system at the Top Of the Atmosphere (TOA) (Forster et al., 2021; Sherwood et al., 2015). The radiative effect induced by a perturbation is classically quantified using RF. The nature of the forcing agent determines the extent to which an instantaneous RF ultimately affects Global Surface Air Temperature (GSAT), the standard metric to measure warming in the climate system. The climate response can be decomposed as: (a) atmospheric adjustments that occur independently of any change in GSAT, and (b) feedbacks that arise through changes in GSAT (Sherwood et al., 2015). Atmospheric adjustments can substantially modify the water content, cloud microphysics, and/or the atmospheric circulation, so that they may end up strongly attenuating or enhancing the initial RF. Without robust estimates of these atmospheric adjustments, the climate impact of both unintentional aviation-driven cirrus formation and deliberate CCT cannot be reliably constrained.

Quantifying adjustments requires filtering out the internal variability of the atmosphere, especially in terms of cloudiness. Amplifying the perturbation is one possible strategy to increase the signal-to-noise ratio when estimating the climate response to a forcing in a climate model. It is imperfect as it assumes linearity between the forcing and the atmospheric response. The extent to which adjustments depend on the intensity of the RF is still an open question for many perturbations. For contrail cirrus, a model study found that atmospheric adjustments reduce the instantaneous RF by more than a factor two (Bickel et al., 2020). However, to obtain statistically significant results, the authors had to artificially amplify air traffic projections for 2050 by a factor of 12, which corresponds to about 36 times present-day air traffic. More recently, a model study by Schumann and Seifert (2025) demonstrated that the RF from contrail cirrus, estimated from two parallel experiments, becomes indistinguishable from atmospheric variability after only a few days. A common feature of these previous studies is their reliance on sustained perturbations, in which the imposed RF and the climate system response are superimposed, complicating the separation of atmospheric adjustments from the evolving model trajectory. In addition, the inherently chaotic nature of the climate system causes unperturbed and perturbed simulations to diverge over time, further hindering a robust attribution of the response.

This study differs from previous studies in two fundamental ways. First, we apply a *pulse perturbation* rather than a sustained perturbation to isolate and quantify atmospheric adjustments. Second, we adopt an alternative strategy to increase the signal-to-noise ratio in dedicated cirrus perturbation experiments by generating an *ensemble of simulation pairs*—control and perturbed—to quantify in a statistically robust way the atmospheric adjustments following the pulse perturbation. That perturbation consists in instantaneously forming cirrus clouds in cloud-free, Ice-SuperSaturated Regions (ISSRs). ISSRs are air masses where water vapor exists in a thermodynamically metastable state as its partial pressure exceeds the saturation pressure with respect to ice (Gierens et al., 2020; Lamquin et al., 2012; Sanogo et al., 2024). These regions not only provide favorable conditions for the formation of natural cirrus clouds (Gierens, 2012), but also allow linear contrails to form, grow, and spread, eventually evolving into contrail cirrus (Kärcher, 2018; Wolf et al., 2023). This experimental design allows us to identify and quantify the global atmospheric adjustments that occur as the properties of ISSRs relax back toward those of the unperturbed state.

This article is organized as follows. Section 2 introduces the notions of climate adjustments, feedbacks and efficacy in response to a given RF. Section 3 first describes the climate model ICOLMDZ, which is a combination of the IPSL General Circulation Model (GCM) LMDZ and the dynamical core DYNAMICO, used to simulate ISSRs and cirrus cloud formation, outlines the methods for implementing the cirrus cloud perturbation using an

21698996, 2026, 8, Downloaded from https://agupubs.onlinelibrary.wiley.com/doi/10.1029/2025JD046235 by NICE, National Institute for Health and Care Excellence, Wiley Online Library on [30/04/2026]. See the Terms and Conditions (https://onlinelibrary.wiley.com/terms-and-conditions) on Wiley Online Library for rules of use; OA articles are governed by the applicable Creative Commons License

21698996, 2026, 8, Downloaded from https://agupubs.onlinelibrary.wiley.com/doi/10.1029/2025JD046235 by NICE, National Institute for Health and Care Excellence, Wiley Online Library on [30/04/2026]. See the Terms and Conditions (https://onlinelibrary.wiley.com/terms-and-conditions) on Wiley Online Library for rules of use; OA articles are governed by the applicable Creative Commons License

ensemble of perturbed and unperturbed simulations, and describes the method used to reduce a cold temperature bias in ICOLMDZ. Section 4 presents the unperturbed ISSR climatology, describes the mechanisms of atmospheric adjustments to cirrus formation and their impact on the atmospheric state, and quantifies the degree of linearity of the adjustments to the intensity of the initial perturbation. Finally, Section 5 concludes the study.

2. Adjustments and Feedbacks

In this section, we briefly review the current theoretical framework of the forcing-response-feedback paradigm that underpins climate change modeling, following the approach outlined by Sherwood et al. (2015) and Forster et al. (2021). In response to an external forcing $d\mathcal{E}(t)$, the climate system evolves toward a new radiative equilibrium by changing the net rate of energy loss at TOA $d\mathcal{R}(t)$ such that

$$\mathcal{N}(t) = d\mathcal{E}(t) - d\mathcal{R}(t)\,, \tag{1}$$

where $\mathcal{N}$ denotes the net radiative imbalance at TOA (with downward radiation counted positive). The new equilibrium is characterized by

$$\overline{\mathcal{N}} = d\overline{\mathcal{E}} - d\overline{\mathcal{R}} = 0\,, \tag{2}$$

where the overlines denote the quantities in their new stationary state. The climate system primarily adjusts $d\overline{\mathcal{R}}$ toward a new equilibrium by changing the global surface temperature, quantified here as the change in GSAT $d\overline{T}$. By taking the total differential of the response-driven loss term with respect to $\overline{T}$, Sherwood et al. (2015) obtain

$$d\overline{\mathcal{R}} = \left(\frac{\partial \overline{\mathcal{R}}}{\partial \overline{T}} + \sum_i \frac{\partial \overline{\mathcal{R}}}{\partial \overline{X_i}} \frac{\partial \overline{X_i}}{\partial \overline{T}}\right) d\overline{T} \equiv -\alpha\, d\overline{T}\,, \tag{3}$$

where the index i runs over the complete set of variables that depends on a GSAT change X. When summed, these contributions form the feedback parameter α, up to sign. By combining (2) and (3), one derives

$$d\overline{T} = \lambda\, d\overline{\mathcal{E}}\,, \tag{4}$$

where the climate sensitivity is defined as $\lambda = -1/\alpha$. It is common to introduce the concept of *efficacy* when comparing the climate sensitivity to a given forcing mechanism to that of CO_2 forcing, historically defined for a doubling of CO_2 concentrations (Hansen et al., 1984, 2005). Formally, we write

$$d\overline{T} = r\lambda_{CO_2}\, d\overline{\mathcal{E}}\,. \tag{5}$$

The value of the efficacy r is sensitive to the characteristics of the forcing mechanism and to the spatial distributions of both the forcing itself and the climate system's response (Rugenstein et al., 2016). The external forcing $d\mathcal{E}(t)$ in (2) includes both the RF of the forcing agent and any response of the atmosphere that does not depend on the subsequent change in surface temperature. These atmospheric changes that are not mediated by the surface temperature change are called *adjustments*. Following the expansion of the GSAT of Equation 2 by Quaas et al. (2024), we write the external forcing $d\mathcal{E}(t)$ as

$$d\mathcal{E}(t) = d\mathcal{F}(t) + \sum_{\text{adj}} d\mathcal{A}_{\text{adj}}(t) + \int \frac{d^2\Omega}{4\pi} \beta_{\text{adj}}(\theta,\phi)\, dT(t,\theta,\phi)\,, \tag{6}$$

where the integration is performed over the solid angle $d^2\Omega = d\phi\, d\theta \cos\theta$, with θ the latitude and ϕ the longitude, $d\mathcal{F}(t)$ is the RF, $d\mathcal{A}_{\text{adj}}$ refers to atmospheric adjustments adj, $dT(t,\theta,\phi)$ is the local surface air temperature change, with θ the latitude and ϕ the longitude, and β_{adj} represents the dynamical adjustment parameters which depend on $dT(t,\theta,\phi)$ with $d\overline{T} = 0$, and is defined analogously to α. In (6), we exclude adjustments that do not affect Earth radiation budget as discussed in Quaas et al. (2024). The external forcing

Table 1
Published Estimates of Contrail Cirrus Efficacy and Related Metrics

Study	Method	Contrail	Related quantity	Efficacy
Ponater et al. (2005)	30-year coupled simulations with 20 × 2,050 aviation	Linear	$\lambda = 0.43\,\mathrm{K\,W^{-1}m^2}$	$r_{\mathrm{RF}} = 0.59$
Rap et al. (2010)	40-year coupled simulations with 100 × 2,000 aviation	Linear	$\lambda = 0.3\,\mathrm{K\,W^{-1}m^2}$	$r_{\mathrm{RF}} = 0.31$
Bickel et al. (2020)	25-year fixed-SST experiment	Contrail cirrus	$\kappa = 0.37 \pm 0.15$	N/A
Lee et al. (2021)	Synthesis study	N/A	Combined value of 0.42 (see text)	
Ponater et al. (2021)	Further analysis of Bickel et al. (2020) simulations	N/A	$\kappa = 0.42 \pm 0.24$	N/A
Bickel et al. (2025)	40-year coupled simulations, with 12 × 2,050 aviation	Contrail cirrus	$\kappa = 0.55 \pm 0.32$	$r_{\mathrm{RF}} = 0.21,\ r = 0.38$

Note. The table highlights differences in methods, contrail implementations, reported quantities and the related efficacy, if applicable. λ is the climate sensitivity (defined in (4)), κ is the ERF to RF ratio, r_{RF} is the RF-based efficacy (defined in (7)), and r is the ERF-based efficacy (defined in (5)). κ values for Bickel et al. (2020), Ponater et al. (2021), and Bickel et al. (2025) are reported with one standard deviation uncertainty range.

defined in (6) is called Effective Radiative Forcing (ERF) and it includes all the atmospheric adjustments (Boucher et al., 2013; Myhre et al., 2013).

In practice it may be difficult to provide an exact estimate of the ERF as defined in (6), since there is a blurred boundary between adjustments and feedbacks. Adjustments occur on time scales ranging from a few minutes for ice crystal formation in linear contrails, for instance, to a season for changes in snow melt caused by soot deposition. Surface temperature response typically occurs on time scales of years to centuries as it involves both the surface and deep oceans. If the RF evolves in time (as it is currently the case), there is always a superposition between adjustments from recent changes in the forcing and feedbacks from the past history of the forcing. Given the complexity involved with the separation of adjustments and feedbacks, estimated ERF values are always an approximation as reviewed in Forster et al. (2021).

The efficacy r (5) is expected to be closer to unity than r_{RF},which is defined from $\mathcal{F}(t)$ without adjustments. Both quantities are related by

$$r = \frac{\mathcal{F}}{\mathcal{E}} \frac{\mathcal{E}^{\mathrm{CO_2}}}{\mathcal{F}^{\mathrm{CO_2}}} r_{\mathrm{RF}}\,. \tag{7}$$

As discussed by Ponater et al. (2021), approximating r_{RF} by $\mathcal{E}/\mathcal{F}$ is inappropriate because (a) $\mathcal{E}^{\mathrm{CO_2}}/\mathcal{F}^{\mathrm{CO_2}}$ is not exactly one (within a 10% range, Richardson et al. (2019)) and (b) r may be far from one for some forcing mechanisms (Marvel et al., 2015; Shine et al., 2012). However the relevance of r_{RF} becomes less because climate models now increasingly estimate the ERF instead of the RF.

For contrail cirrus, Lee et al. (2021) report $r_{\mathrm{RF}} = 0.42$ as the average of three studies. However, these values are not commensurate: Ponater et al. (2005) and Rap et al. (2010) estimate r_{RF} whereas Bickel et al. (2020) report an ERF/RF ratio. Averaging three consistent r_{RF} estimates (Bickel et al., 2025; Ponater et al., 2005; Rap et al., 2010) yields a combined value of 0.37 (see Table 1 for details). The relatively low efficacy likely reflects the spatial distribution of contrail forcing and its vertical structure, which may weakly couple the forcing to surface temperature compared with other agents (Rugenstein et al., 2016; Shindell & Faluvegi, 2009).

No estimates of CCT ERF/RF ratio or efficacy currently exist. Although several studies have quantified RF using climate models (Gasparini et al., 2020; Liu & Shi, 2021; Storelvmo & Herger, 2014), the radiative signal is often indistinguishable from zero (Gasparini & Lohmann, 2016). The cooling from reduced ice crystal number concentration is largely offset by concurrent decreases in ice crystal size, and atmospheric adjustments tend to counteract the intended cooling, with results strongly dependent on poorly constrained ice microphysics Tully et al. (2022).

21698996, 2026, 8, Downloaded from https://agupubs.onlinelibrary.wiley.com/doi/10.1029/2025JD046235 by NICE, National Institute for Health and Care Excellence, Wiley Online Library on [30/04/2026]. See the Terms and Conditions (https://onlinelibrary.wiley.com/terms-and-conditions) on Wiley Online Library for rules of use; OA articles are governed by the applicable Creative Commons License

21698996, 2026, 8, Downloaded from https://agupubs.onlinelibrary.wiley.com/doi/10.1029/2025JD046235 by NICE, National Institute for Health and Care Excellence, Wiley Online Library on [30/04/2026]. See the Terms and Conditions (https://onlinelibrary.wiley.com/terms-and-conditions) on Wiley Online Library for rules of use; OA articles are governed by the applicable Creative Commons License

3. Experimental Setup

3.1. Climate Model and ISSRs Parametrization

We use a version of the ICOLMDZ similar to the one used by Borella et al. (2025). In this study, ICOLMDZ combines version 6A of the atmospheric GCM LMDZ (Boucher et al., 2020; Hourdin et al., 2020; Madeleine et al., 2020) with the DYNAMICO dynamical core (Dubos et al., 2015). The new dynamical core uses an icosahedral grid to avoid numerical instabilities occurring at the poles when solving geophysical fluid dynamics equation on a regular latitude and longitude grid. Finally, the radiative transfer model used in LMDZ6A is a version of RRTM for the LW radiation (Mlawer et al., 1997) and on another parametrization for SW radiation (Fouquart & Bonnel, 1980).

In this study, the model configuration has 95 vertical layers of varying thickness. At the tropopause level, the vertical grid spacing is about 500 m. The horizontal grid in DYNAMICO corresponds to dividing the edges of an icosahedron into 40 equal segments, resulting in a model grid spacing of roughly $\Delta x = 250$ km. The dynamical core operates with a timestep of 450 s, while the physical processes in LMDZ use a 15-min timestep. The radiation timestep is also fixed to 15 min to capture the radiative impact of fast changes in atmospheric variables. Output data is saved every 30 min as a time-averaged value.

The original version of LMDZ6A cannot simulate cloud-free, ISSRs in the upper atmosphere, as ice cloud formation is triggered at saturation. Here, we use a new cloud parametrization that allows supersaturation of the water vapor with respect to ice, as described in Borella et al. (2025). This parametrization of cirrus cloud is activated only for air temperatures below 235 K for which homogeneous freezing of solution droplets dominates. As a consequence, ISSRs form mostly between 300 hPa and 200 hPa in mid-latitudes.

Each grid cell is partitioned into a cloudy fraction, χ_{cld}, and a cloud-free fraction. The cloud-free fraction is further subdivided into subsaturated and supersaturated fractions, denoted χ_{sub} and χ_{issr}, respectively.

$$\chi_{\mathrm{cld}} + \chi_{\mathrm{sub}} + \chi_{\mathrm{issr}} = 1\,. \tag{8}$$

The cloud fraction is denoted by the subscript cld and the cloud-free fraction is split into a water-vapor subsaturated cloud-free fraction, denoted sub, and a water-vapor supersaturated cloud-free fraction, denoted issr. The total water content in the cell, q_{tot}, is split accordingly among the gridbox averages q_{cld}, q_{sub}, and q_{issr}.

A cloud-free parcel is sub-saturated when the water vapor specific humidity q is lower than the ice saturation specific humidity $q_{\mathrm{sat,ice}}(T)$, which is calculated as the saturation vapor pressure over a flat ice surface at temperature T. If $q > q_{\mathrm{sat,ice}}(T)$, the air parcel is ice super-saturated. If the humidity rises above $q > \gamma_{ss} q_{\mathrm{sat,ice}}(T)$, where γ_{ss} is a dimensionless quantity, homogeneous freezing occurs, and the vapor in the ISSR condenses into ice. γ_{ss} can be approximated by a function of temperature only (Koop et al., 2000; Ren & Mackenzie, 2005). The in-cloud water content $\overline{q}_{\mathrm{cld}} = q_{\mathrm{cld}}/\chi_{\mathrm{cld}}$ is split into in-cloud water vapor $\overline{q}_{\mathrm{vap}}$ and in-cloud ice water content $\overline{q}_{\mathrm{cond}}$, such that

$$\overline{q}_{\mathrm{cld}} = \overline{q}_{\mathrm{vap}} + \overline{q}_{\mathrm{cond}}\,. \tag{9}$$

The separation between vapor and ice in the cloud is dictated by the rate of sublimation of ice crystals and that of condensation of vapor into ice, absorbing and releasing latent heat, respectively. Finally, if the specific humidity within the cloud drops below $q_{\mathrm{sat,ice}}(T)$, the cloud can dissipate and the corresponding grid fraction becomes subsaturated clear sky. In-cloud relative humidity is not prescribed to 100% so $\overline{q}_{\mathrm{vap}}$ can be different from $q_{\mathrm{sat,ice}}(T)$.

The parametrization uses a one-moment microphysical scheme for which the microphysical cloud properties are determined only from the prognostic ice water content. It implies that the ice crystal number concentration is not tracked by the model and is prescribed for each process. Ice crystal sedimentation is governed by an auto-conversion rate described by Madeleine et al. (2020) as

$$\frac{d\overline{q}_{\mathrm{cond}}}{dt} = \frac{1}{\rho}\frac{\partial}{\partial z}\left(\rho\, w_{iw}\, \overline{q}_{\mathrm{cond}}\right), \tag{10}$$

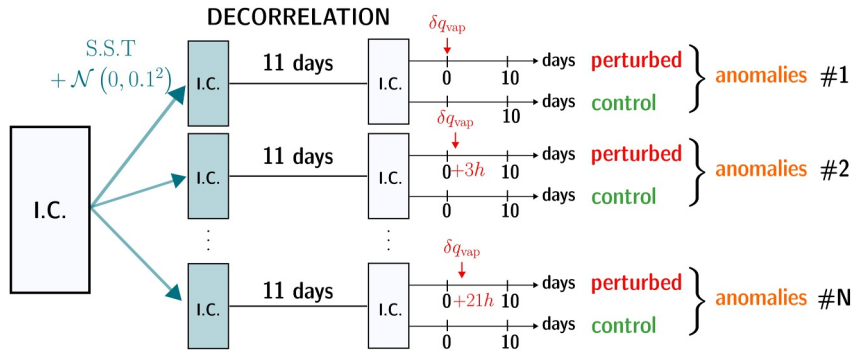

Figure 1. Schematic of the generation of the N-pair ensemble. We start from a common set of initial conditions (ICs) and perturb the SST field. After a decorrelation period of 11 days, the new atmospheric ICs are independent and serve to generate pairs of control and perturbed simulations. The difference between these two simulations provides anomalies. The perturbation time is spread over the first day, spaced by 3 hours, thus spanning eight different initializations for the perturbation. See main text for details.

where ρ is the air density, $w_{iw} = \gamma_{iw} w_0$ is the fall velocity, γ_{iw} is a tuning factor, and $w_0 = 3.29\left(\rho\,\overline{q}_{\text{cond}}\right)^{0.16}$ (Heymsfield & Donner, 1990). The extension to a two-moment microphysical scheme will be the subject of future work, and requires to consider the various sources and sinks of ice crystals (Proske et al., 2023).

The same set of parameters presented by Borella et al. (2025) is used in this study, since they concluded that simulations using ICOLMDZ with this configuration show good agreement against ISSR observations at local and global scales. A fine-tuning of the parametrization will be subject of future works.

3.2. Ensemble Design and Perturbation Implementation

Determining the ERF associated with a high-level cloud perturbation in a GCM is challenging. This difficulty arises because the radiative impact of cirrus induced by aviation or CCT is small compared to the variability in net radiative flux (with variations in cloudiness contributing the most to this variability). One solution is to amplify the signal drastically, but that makes interpreting the results difficult because forcing and adjustments are not a linear function of the water budget perturbation, as noted by Bickel et al. (2020, 2025). Another solution is to reduce the statistical impact of atmospheric variability.

We do so by constructing an ensemble of N simulation pairs, as illustrated in Figure 1. For each pair, we apply a small random Gaussian perturbation of 0.1 K to the sea surface temperature (SST) field of the initial conditions (ICs) in each gridbox, followed by a 11-day decorrelation period to decorrelate the simulations from each other (see Figure S2 in Supporting Information S1). The imposed SST field is fixed to a climatological average. This perturbation of the ICs aims to position the model onto different trajectories to sample different situations. Perturbing the SST field rather than the vertical temperature profile has the advantage of keeping the whole climate system consistent and numerically stable. This approach also allows to generate an arbitrary number of simulation pairs to improve statistics. In this study, the statistical significance of our results is quantified using a two-tailed Student's t-test with a critical probability of $p = 5\%$ to exclude responses statistically indistinguishable from zero, unless where stated otherwise. This enables us to extract clear and statistically significant signals from the background atmospheric variability.

In each pair of simulations, the perturbed simulation is subject to a global cirrus cloud perturbation, while the control simulation remains unperturbed. Since the time of day of the imposed perturbation may affect the magnitude of the RF and its adjustments, we sample different times of day by offsetting the perturbation time by three hours between successive ensemble members. Taken together, the ensemble members span $24/3 = 8$ different times of day for the imposed perturbations. In the following, results are obtained by averaging all ensemble members together, and are presented in terms of absolute difference relative to the perturbation time. In this study, we consider two periods of the year: the perturbation occurs either on 11th January, or on 11th July in order to study seasonal variability.

21698996, 2026, 8, Downloaded from https://agupubs.onlinelibrary.wiley.com/doi/10.1029/2025JD046235 by NICE, National Institute for Health and Care Excellence, Wiley Online Library on [30/04/2026]. See the Terms and Conditions (https://onlinelibrary.wiley.com/terms-and-conditions) on Wiley Online Library for rules of use; OA articles are governed by the applicable Creative Commons License

21698996, 2026, 8, Downloaded from https://agupubs.onlinelibrary.wiley.com/doi/10.1029/2025JD046235 by NICE, National Institute for Health and Care Excellence, Wiley Online Library on [30/04/2026]. See the Terms and Conditions (https://onlinelibrary.wiley.com/terms-and-conditions) on Wiley Online Library for rules of use; OA articles are governed by the applicable Creative Commons License

Table 2
Summary of Simulations, Including Their Description, Nudging Configuration, Ensemble Size (N), and Initialization Dates

Name	Description	Nudging	N	Init. date
Unnudged	Unnudged simulation	None	10	11th Jul
Nudged	Simulation nudged toward ERA5	Soft nudging of T and P_s	10	11th Jul
Control	Control simulation	Soft nudging of T and P_s	50	10th Jan
				11th Jul
Locally perturbed	Simulation with a pulse perturbation restricted to [30°N, 60°N]	Soft nudging of T and P_s	50	11th Jan
				11th Jul
Globally perturbed	Simulation with a pulse, global perturbation	Soft nudging of T and P_s	50	11th Jan
				11th Jul
Global, $f = 0.5$	Simulation with a global conversion of 50% of the ISSRs	Soft nudging of T and P_s	50	11th Jan
Global, $f = 0.1$	Simulation with a global conversion of 10% of the ISSRs	Soft nudging of T and P_s	50	11th Jan
Global, $f = 0.05$	Simulation with a global conversion of 5% of the ISSRs	Soft nudging of T and P_s	150	11th Jan
Global, $f = 0.01$	Simulation with a global conversion of 1% of the ISSRs	Soft nudging of T and P_s	150	11th Jan

Note. All listed simulations are run for 10 days. T stands for the air temperature and P_s for the surface pressure.

The perturbation to the cirrus cloud properties applied in this study consists of a pulse (i.e., one-off instantaneous) global conversion of all cloud-free, ISSRs into cirrus clouds. The initial objective of this idealized experiment was to analyze the subsequent adjustments occurring over a duration of ten days, though our analysis of adjustment timescales will show that four days is enough. At a given timestep and only once, we perturb the system, by converting water vapor in the ISSR into cloud total water content such that

$$q_{\mathrm{cld}} := q_{\mathrm{cld}} + q_{\mathrm{issr}}\,, \tag{11}$$

where these three quantities are grid-box averages. Thus, the supersaturated cloud-free fraction becomes zero and the grid-box fractions are adjusted accordingly

$$\chi_{\mathrm{cld}} := 1 - \chi_{\mathrm{clr}}\,, \qquad \chi_{\mathrm{issr}} := 0\,. \tag{12}$$

The humidity added to the cloud fraction is split between the vapor and ice phases. The humidity which is below saturation is kept in vapor phase

$$q_{\mathrm{vap}} := q_{\mathrm{vap}} + q_{\mathrm{sat}}\chi_{\mathrm{issr}}\,, \tag{13}$$

where q_{vap} is the gridbox-averaged water vapor specific humidity. The condensed water is added to the ice water content so that our perturbation conserves total water. Despite the large perturbation to the upper-atmospheric water budget caused by the conversion of all ISSRs into cirrus clouds, the radiative response is not expected to be much larger than timestep-to-timestep variations in the radiative budget, which is why the approach is based on an ensemble of simulations.

As discussed in Section 2, adjustments imply the absence of changes in global surface air temperature changes. This condition is met in our method because we focus on the very short-term behavior of the system, during which GSAT remains effectively constant.

The pulse perturbation is applied over different regions of the atmosphere in this study. In Sections 4.2 and 4.4, the perturbations are global while, in Section 4.3, we discuss the difference between simulations with regional and global perturbations. Indeed, in the case of contrail cirrus, the increase of high-level cloudiness is confined in the northern mid-latitudes, [30°N, 60°N], where most of the air traffic occurs (Dannet et al., 2024; Teoh et al., 2024), which we represent by a perturbation restricted to a 30°N − 60°N latitude range. The set of simulations is

summarized in Table 2. The simulation ensembles labeled "Unnudged" and "Nudged" are used in Section 3.3 to demonstrate the effects of the nudging setup.

3.3. Nudging Setup

Many GCMs suffer from a persistent cold bias in the upper atmosphere (Gettelman et al., 2010; Hourdin et al., 2020). It is also the case in our control simulations where the temperature at 200 hPa is locally up to 3 K colder than in the ERA5 reanalysis (Hersbach et al., 2020). This cold bias matters because the saturation vapor pressure is highly sensitive to air temperature. At the tropopause level, a 3 K cold bias in temperature reduces saturation vapor pressure by 30% according to the Clausius-Clapeyron relation. Consequently, the bias may reduce the amount of ice water content generated by the perturbation.

In this study, this bias is corrected using an online bias correction technique, or *soft nudging* (Kharin & Scinocca, 2012; Krinner et al., 2020). Soft nudging uses a standard nudged run to diagnose a time varying tendency, then replays only the multi year, diurnally and seasonally varying mean of that tendency in the actual experiments. The rationale for using the soft nudging is to preserve the physics of adjustments—such as the release of latent heat—which would be hindered by a standard temperature nudging approach. The soft nudging relies on a two-step procedure, involving both the air temperature and surface pressure. Nudging the surface pressure is necessary because the commonly used state variable quantifying temperature in GCMs is the potential temperature, which is conserved during dry air adiabatic processes (Baumgartner et al., 2020). In what follows, we focus on the treatment of temperature, as surface pressure follows the same procedure.

We use the standard nudging procedure where the temperature field $T(\vec{r},t)$ is modified using a Newtonian relaxation toward the ERA5 values $T_{\mathrm{ERA5}}(\vec{r},t)$ at any point $\vec{r}$ of the atmosphere and time t (Jeuken et al., 1996). Formally,

$$\frac{\partial T(\vec{r},t)}{\partial t} = \hat{F}T(\vec{r},t) - \frac{T(\vec{r},t) - T_{\mathrm{ERA5}}(\vec{r},t)}{\tau}, \tag{14}$$

where the operator $\hat{F}$ represents the time evolution from the climate model and τ is the relaxation time. The second term on the right-hand side is the nudging rate, which brings T toward T_{ERA5}. We choose to run the simulation over $n = 10$ years and the relaxation time is set to $\tau = 1$ day.

The soft nudging consists in reinjecting the time-average of the relaxation term $\widetilde{\Delta T}(\vec{r},t)$ while preserving its diurnal and seasonal variations. Formally,

$$\frac{\partial T(\vec{r},t)}{\partial t} = \hat{F}\,T(\vec{r},t) - \frac{\widetilde{\Delta T}(\vec{r},t)}{\tau}. \tag{15}$$

We first define the multi-year average of the relation term

$$\overline{\Delta T}(\vec{r},t) = \frac{1}{n}\sum_{y=1}^{n} \Delta T_y(\vec{r},t), \tag{16}$$

where $\Delta T_y(\vec{r},t) = T(\vec{r},t) - T_{\mathrm{ERA5}}(\vec{r},t)$ with the index y running over years. The average correction $\overline{\Delta T}(\vec{r},t)$ is defined for $t = [1, N_d \cdot 365]$ where $N_d = 192$ is the number of dynamical timesteps in a day and 365 is the number of days in a year as the 366th day of leap years is discarded. However, the nudging rate $\overline{\Delta T}(\vec{r},t)$ remains noisy, as can be seen in Figure 2. Rather than performing a multi-decadal simulation that would be computationally costly, we smooth out the nudging rate $\overline{\Delta T}(\vec{r},t)$ in a way that preserve the diurnal and seasonal cycles. This is done by averaging over a time windows of $\pm N_{\mathrm{days}} = \pm 20$ days following a normal Gaussian distribution centered in zero with standard deviation of $\sigma_{\mathrm{days}} = 5$ days. The value of the static corrections applied to the control and perturbed simulations become thus

21698996, 2026, 8, Downloaded from https://agupubs.onlinelibrary.wiley.com/doi/10.1029/2025JD046235 by NICE, National Institute for Health and Care Excellence, Wiley Online Library on [30/04/2026]. See the Terms and Conditions (https://onlinelibrary.wiley.com/terms-and-conditions) on Wiley Online Library for rules of use; OA articles are governed by the applicable Creative Commons License

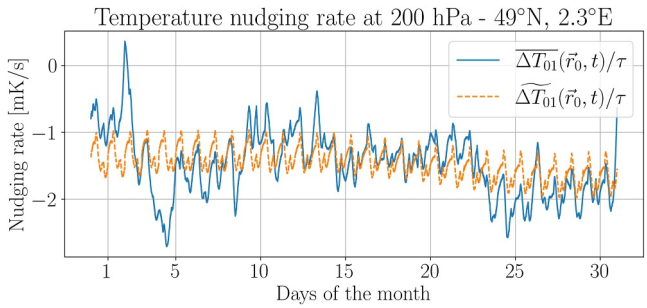

Figure 2. Nudging rate, in mK s^{-1}, from a 10-year simulation nudged toward ERA5 reanalysis for January for the gridbox above Paris at 200 hPa. The nudging rate averaged over 10 years is shown in blue, while the nudging rate further smoothed following (17) is shown in orange.

$$\widetilde{\Delta T}(\vec{r},t) = \sum_{j=-N_{\text{days}}}^{N_{\text{days}}} \omega(j)\,\overline{\Delta T}(\vec{r},t+j\cdot N_{\text{d}}), \tag{17}$$

where $\omega(j)$ are the Gaussian weights such that $\sum_j \omega(j) = 1$. As the data set represents a 10-year climatology and does not correspond to a specific year, the temporal index is defined cyclically for data access, such that 1st January follows 31st December. The temperature nudging rate are successfully smoothed as shown in orange in Figure 2 with a clear diurnal cycle.

The averaged and smoothed temperature and surface pressure nudging rate are then used in reference and perturbed simulations. In Figure 3, we present the vertical temperature profile of both the reference and soft-nudged simulations compared to ERA5 reanalysis, extracted from an ensemble of ten simulations of ten days initialized on 10th July. The standard deviation is computed among the simulations of each ensemble. Figure 3a shows that the cold bias is successfully reduced between the pressure range of 450 hPa and 150 hPa, relevant for contrail and CCT studies. This is confirmed by Figures 3b and 3c that show the temperature histograms at 200 hPa and 250 hPa, respectively.

As this temperature correction could have modified the distribution of ISSRs and the radiative balance of the climate system, we have checked the climatology of the simulations with soft nudging. Comparisons against CERES (Loeb et al., 2009), CALIPSO (Chepfer et al., 2010), and IAGOS (Petzold et al., 2015) show that the TOA radiative budget, cirrus cloud cover, and ISSRs remain well simulated without the need for a retuning (see Figure S1 in Supporting Information S1).

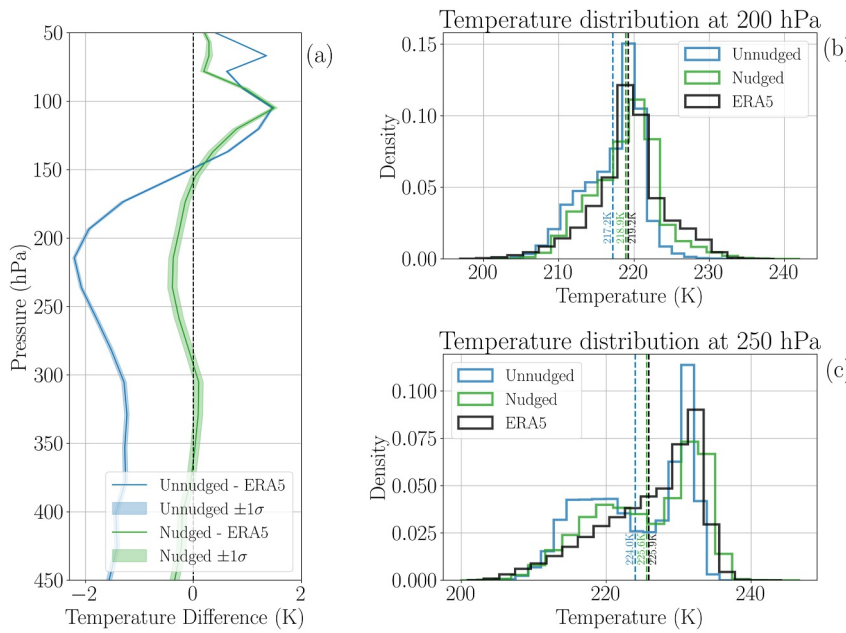

Figure 3. Correction of the air temperature vertical profile using soft-nudging in temperature and surface pressure using nudging rate $\widetilde{\Delta T}(\vec{r},t)/\tau$ defined in (17). (a) Deviation of the temperature profiles averaged over a 10 days period from the unnudged simulation (blue) and the nudged simulation (green) ensembles, both initialized on 10th July, compared to ERA5 data averaged over July 2007. The envelope represents one standard deviation computed over the ensemble of simulation pairs with $N = 10$. (b) Histogram of the temperature at 200 hPa. (c) Histogram of the temperature at 250 hPa. The dashed vertical lines in panels (b, c) represent the mean values.

21698996, 2026, 8, Downloaded from https://agupubs.onlinelibrary.wiley.com/doi/10.1029/2025JD046235 by NICE, National Institute for Health and Care Excellence, Wiley Online Library on [30/04/2026]. See the Terms and Conditions (https://onlinelibrary.wiley.com/terms-and-conditions) on Wiley Online Library for rules of use; OA articles are governed by the applicable Creative Commons License

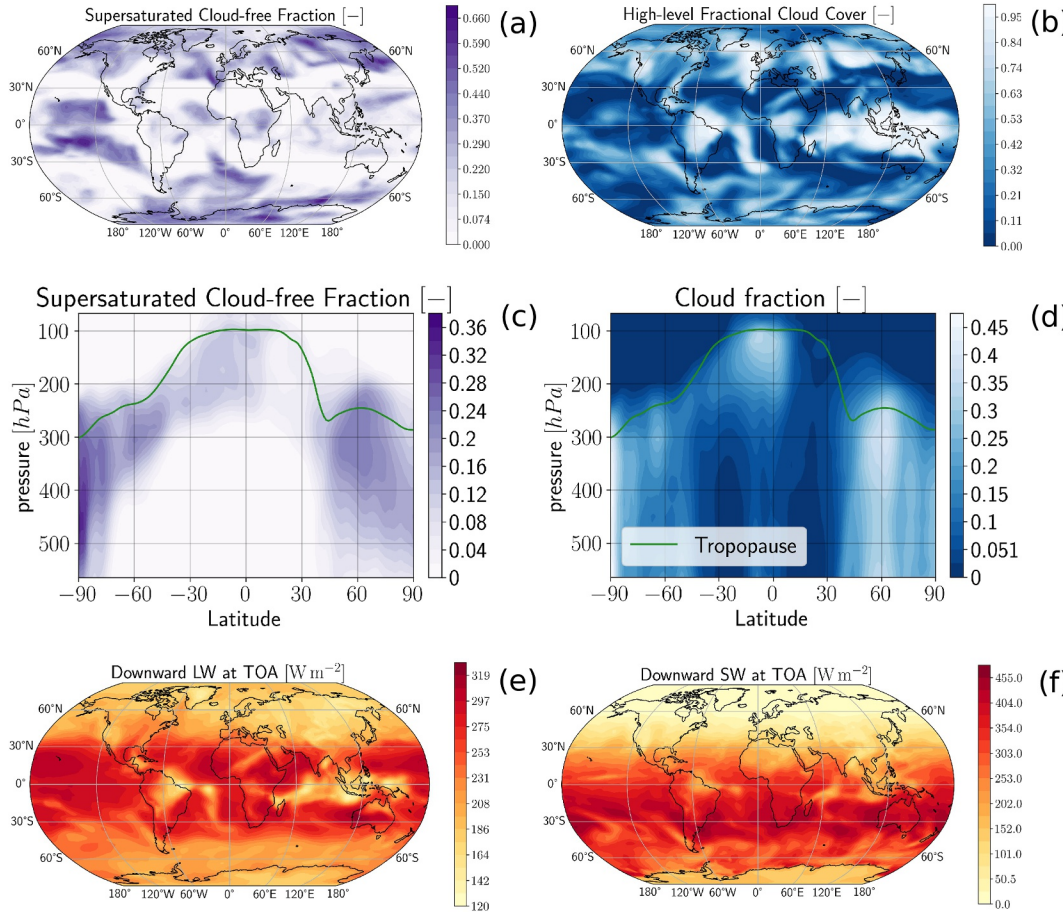

Figure 4. Ensemble-mean of key variables of the simulated climate over one day before the perturbation on 10th January. The model variables are averaged over one day and over $N = 50$ simulations. Distribution of (a) the supersaturated cloud-free fraction at the tropopause, (b) the high-level fractional cloud cover, (e) the net outgoing LW radiation at TOA, in W m^{-2}, and (f) the net downward SW radiation at TOA, in W m^{-2}. Zonally averaged cross-section of (c) the supersaturated cloud-free fraction and (d) the cloud fraction.

4. Results

4.1. Climate System Before the Perturbation

Figures 4 and 5 show the climatological distributions of the high-level fractional cloud cover (cloud fraction above $p < 440$ hPa), the cloud-free, supersaturated fraction, and the SW and LW radiation at TOA as an ensemble-mean averaged over one day before the perturbation occurs on 10th January and on 10th July, respectively.

4.2. Sequence and Mechanisms of the Cirrus Cloud Perturbation

Distributions and time evolution of model variables are analyzed in details using the simulations initialized on 10th January, discussed in Section 4.2.1, and Jul. 10th, discussed in Section 4.2.2. Results are presented in a way that follows the sequence of the mechanisms involved in the cirrus cloud perturbation and adjustments. The perturbation initially increases ice water path (IWP), thereby inducing a RF and leading to the adjustment of upper-atmospheric humidity. Over time, the additional ice crystals sediment, which dehydrates the UT but humidity is then replenished by transport from lower levels, with the model variables progressively returning to their unperturbed statistics. These anomalies represent the adjustments we aim to characterize. We note that the 2D fractional cloud cover is estimated from model-level cloud fractions using the maximum-random overlap assumption. In what follows, the term upper atmosphere refers to atmospheric layers where the pressure is below

21698996, 2026, 8, Downloaded from https://agupubs.onlinelibrary.wiley.com/doi/10.1029/2025JD046235 by NICE, National Institute for Health and Care Excellence, Wiley Online Library on [30/04/2026]. See the Terms and Conditions (https://onlinelibrary.wiley.com/terms-and-conditions) on Wiley Online Library for rules of use; OA articles are governed by the applicable Creative Commons License

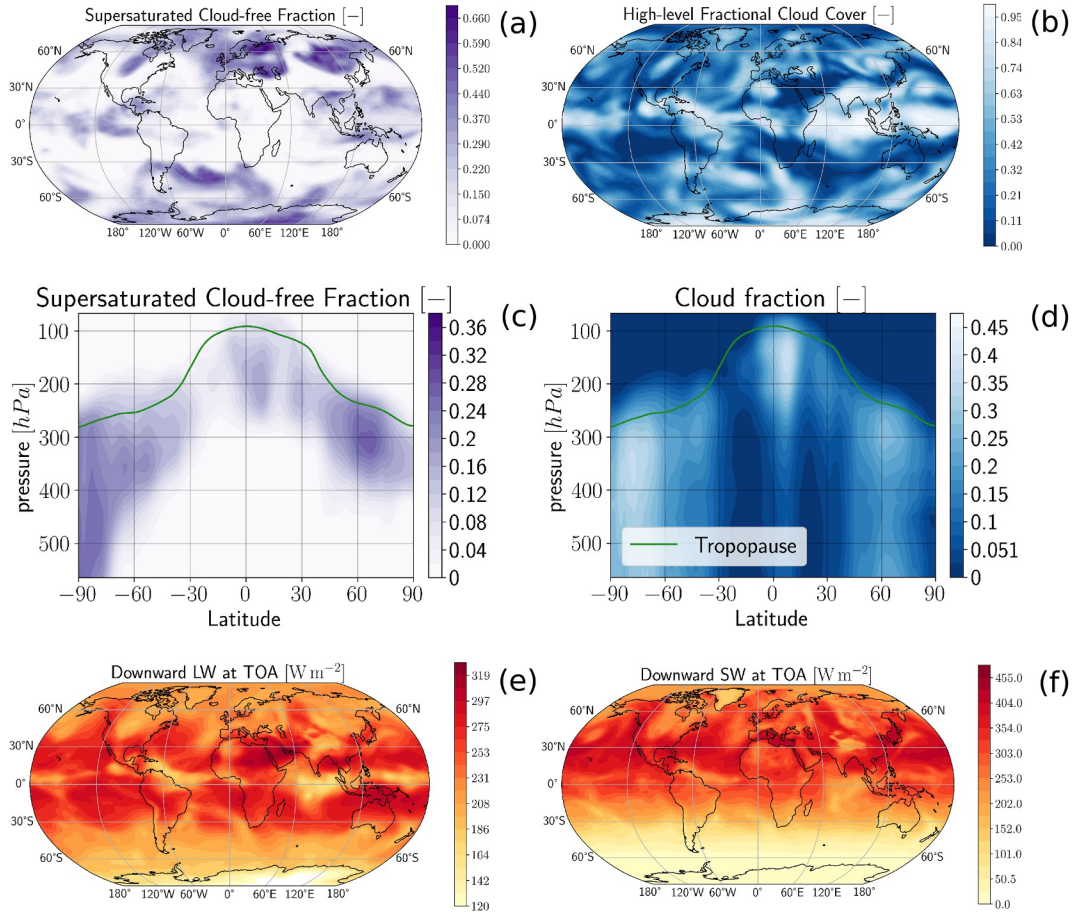

Figure 5. As Figure 4 but for simulations initialized on 10th July.

440 hPa. This includes the stratosphere but it is of no consequence on the model variables studied in this Section because there are few ISSRs in the stratosphere.

4.2.1. Simulations Initialized on 10th January

As expected, the perturbation introduced in the simulation leads to a substantial increase in high-level fractional cloud cover one hour after the perturbation, as illustrated in Figure 6. An absolute local increase of up to 66% is seen in Figure 6a. Figure 6b shows that ice cloud formation is concentrated around the tropopause and down to 300 hPa below the tropopause level. The ice cloud anomaly extends to vertical levels below the typical altitude range of the ISSR distribution (Figure 4c) which is explained by a rapid sedimentation of ice crystal within one hour after the perturbation. A consequent amount of ice is formed as seen in Figure 6c where the anomaly of the upper atmospheric IWP locally reaches up to 33 g m^{-2}, which corresponds to a 300% increase. Newly formed ice crystals are seen over the same pressure range than cloud fraction anomaly as seen in Figure 6d.

After only few hours, the high-level fractional cloud cover strongly decreases and switches to a negative anomaly compared to the control simulation after about five hours, as shown in Figure 7a. It corresponds to a previous effective cirrus cloud lifetime estimate of 6 hours in the tropical tropopause region (Gasparini et al., 2017). It is also interesting that the timescale of the high-level cloud cover anomaly approximately matches the mean contrail lifetime of 4.5 hours estimated by Kärcher and Corcos (2025) in their model. This can be explained by cirrus cloud and contrail cirrus being governed by similar physical processes. Nevertheless our pulse experiment also shows that the subsequent negative anomaly persists for up to four days. As shown in Figure 7b, this phenomenon occurs over the whole latitude range from 100 hPa above the tropopause level up to 300 hPa below in northern mid-

21698996, 2026, 8, Downloaded from https://agupubs.onlinelibrary.wiley.com/doi/10.1029/2025JD046235 by NICE, National Institute for Health and Care Excellence, Wiley Online Library on [30/04/2026]. See the Terms and Conditions (https://onlinelibrary.wiley.com/terms-and-conditions) on Wiley Online Library for rules of use; OA articles are governed by the applicable Creative Commons License

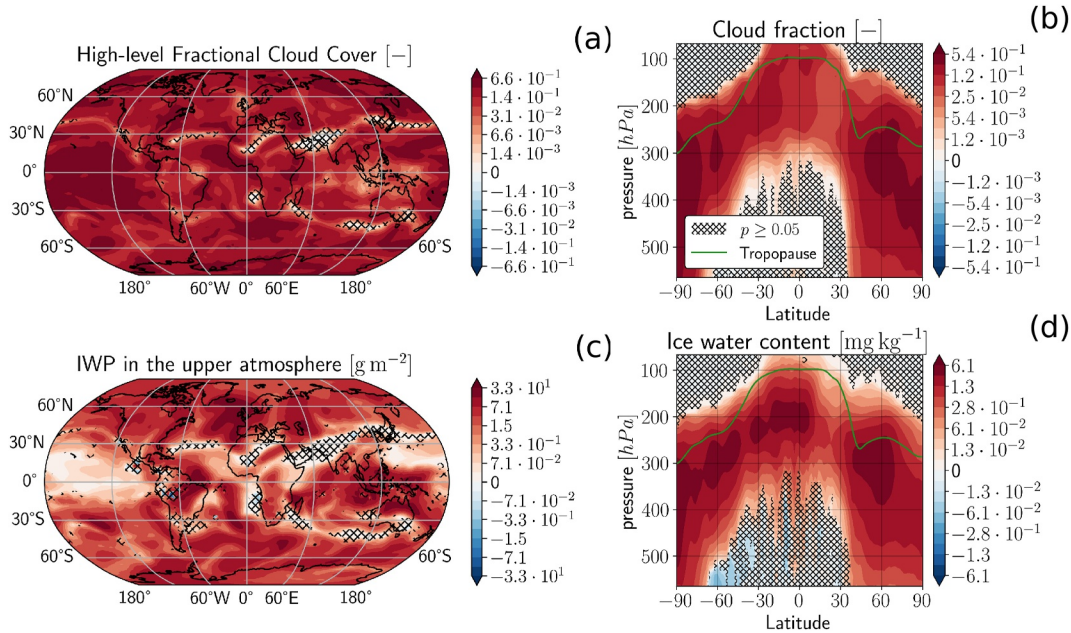

Figure 6. Distribution of the newly formed ice clouds and the associated ice content averaged 1 hour after the perturbation: Distribution of (a) the high-level fractional cloud cover and (c) the IWP, in g m^{-2}, in the upper atmosphere anomalies. Latitude-pressure distribution of the zonally averaged (b) cloud fraction and (d) ice water content, in kg kg^{-1}, anomalies. Data are extracted from an ensemble of $N = 50$ simulation pairs initialized on 10th January. The green, solid lines on the latitude-pressure plots represent the averaged value of the tropopause level. Regions that do not pass a two-tailed Student's *t*-test at 5% level are indicated with hatching. Note the logarithmic scale on the color bar. Thus, relatively small anomalies may be statistically significant.

latitudes. The strongest decrease of about 1% is located in the UTLS, around the tropopause. The high-level cloud cover anomaly induces a radiative imbalance, discussed in more details in Sections 4.3 and 4.4.

Upper-atmospheric IWP exhibits a similar behavior, except that the anomaly disappears after 2.5 days in the polar latitudes of the North Hemisphere as shown in Figure 7c. The perturbation condensed a large amount of water which leads to a big autoconversion rate grows with the amount of ice according to (10). Figure 7d indicates that it only takes a couple of hours for ice water content to decrease at the tropopause level, whereas the ice water content anomaly is still positive at 400 hPa 8 hours after the perturbation. This time lag may be interpreted as an evidence of ice-crystal sedimentation.

Figures 7e and 7f show that the air temperature is increased by tens of millikelvins after the perturbation occurs. The source of this warming is partially explained by the release of latent heat. After the perturbation, the ice water content anomaly reaches 2.9 mg kg^{-1} in Figure 7d, which corresponds to approximately 6 mK of air temperature warming at the tropopause level. In addition, the perturbation induces warming below the tropopause and cooling above it, forming a temperature dipole, as already noted by Bickel et al. (2020). This response is expected to arise from absorption and emission of LW radiation by newly formed ice crystals: absorption dominating below the tropopause, with emission dominating above. However, Figures 7b and 7f suggest that the temperature response lags the cloud response.

Finally, the perturbation is responsible for a long-term drop of water vapor and Relative Humidity with respect to ice, RH_i, shown in Figure 8. It occurs directly after the perturbation and quickly reaches lower altitudes as shown in Figure 8a. It occurs over the same pressure range as the ice cloud formation (see Figure 6b). In Figure 8a, the positive anomaly around 500 hPa in specific humidity turns negative after a couple of hours. We hypothesized that the initial increase is due to sublimation of the ice crystals formed above and sedimented to this level. This is followed by further sedimentation of the ice and the downward propagation of the negative anomaly in specific humidity due to the initial perturbation through mixing.

21698996, 2026, 8, Downloaded from https://agupubs.onlinelibrary.wiley.com/doi/10.1029/2025JD046235 by NICE, National Institute for Health and Care Excellence, Wiley Online Library on [30/04/2026]. See the Terms and Conditions (https://onlinelibrary.wiley.com/terms-and-conditions) on Wiley Online Library for rules of use; OA articles are governed by the applicable Creative Commons License

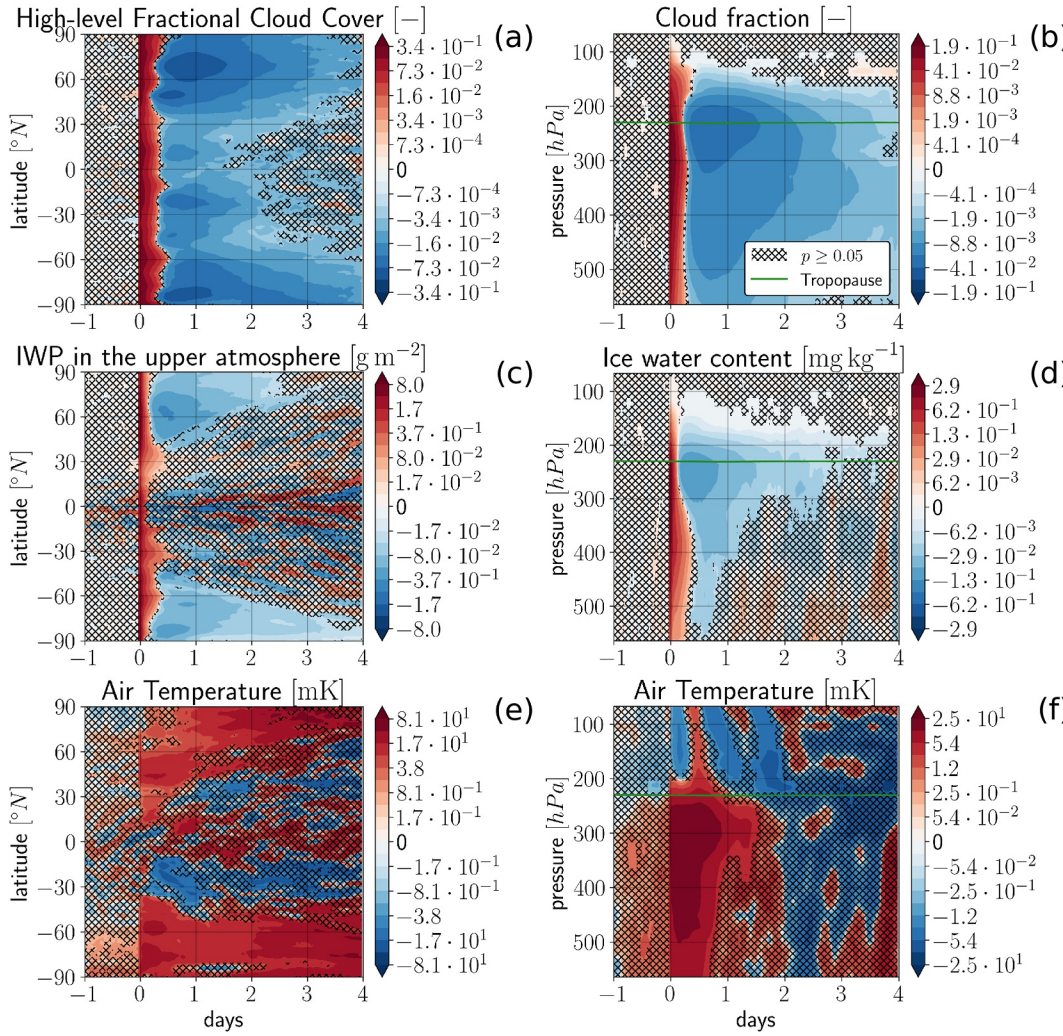

Figure 7. Time evolution of the zonally averaged anomalies of (a) cloud fraction anomaly at the tropopause level, (c) IWP, in g m^{-2}, in the upper atmosphere, and (e) air temperature, in mK, at the tropopause level. Time evolution of vertical profile anomalies averaged over northern mid-latitudes, [30°N, 60°N], of (b) the cloud fraction and (d) the ice water content, in mg kg^{-1}, and (f) the air temperature, in mK. Data extracted from an ensemble of $N = 50$ simulation pairs initialized on 11th January. Regions that do not pass a two-tailed Student's t-test at 5% level are indicated with hatching. Note the logarithmic scale on the color bar. Thus, relatively small anomalies may be statistically significant.

4.2.2. Simulations Initialized on 11th July

The results in this section are the same as those presented in Section 4.2, beside the fact that the experiments are initialized on 11th July. In what follows, we emphasize the major differences between these two seasons. In general, the physics of the adjustments is the same, but they are confined to a narrower pressure range below the tropopause.

After 1 hour, the high-level fractional cloud cover and the IWP in the upper atmosphere are increased by a similar amount compared to the simulation initialized on 11th January, as shown in Figures 9a and 9c. The IWP distribution in 9c presents some weaker increase regions primarily along 15°S. This weaker increase of both high-level fractional cloud cover and IWP is also located around 20°S in Figures 6b and 6d, respectively. In July (Figures 9b and 9d), this weaker increase is mirrored to 20°N. Figures 9b and 9d shows that, in the Northern Hemisphere, the atmospheric variability screens the signal for pressures larger than 500 hPa. Thus, the response in IWP and high-level fractional cloud cover is confined at higher altitude compared to those in Figures 6b and 6d.

21698996, 2026, 8, Downloaded from https://agupubs.onlinelibrary.wiley.com/doi/10.1029/2025JD046235 by NICE, National Institute for Health and Care Excellence, Wiley Online Library on [30/04/2026]. See the Terms and Conditions (https://onlinelibrary.wiley.com/terms-and-conditions) on Wiley Online Library for rules of use; OA articles are governed by the applicable Creative Commons License

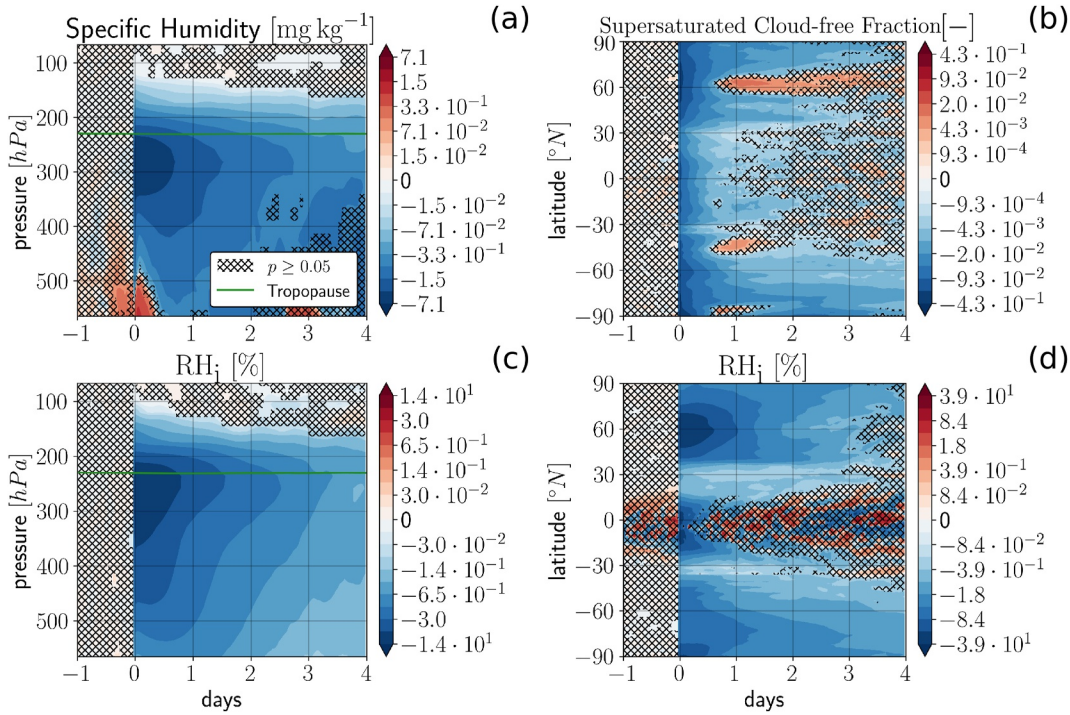

Figure 8. Time evolution of (a) the specific humidity, in mg kg^{-1}, and (c) RH$_i$, in %, anomaly vertical profiles averaged over northern mid-latitudes. Time evolution of the zonally averaged (b) supersaturated cloud-free fraction and (d) RH$_i$, in %, anomaly at the tropopause level. Data extracted from an ensemble of $N = 50$ simulation pairs initialized on 11th January. Regions that do not pass a two-tailed Student's *t*-test at 5% level are indicated with hatching. Note the logarithmic scale on the color bar. Thus, relatively small anomalies may be statistically significant.

Figure 10d confirms that the pressure range over which ice crystals are formed by the perturbation is restricted to [100, 500] hPa. It leads to a broader range of pressure for the high-level fractional cloud cover as it is positive up to 550 hPa in Figure 10b. At 400 hPa, the increase in ice water content persists for approximately half a day and is

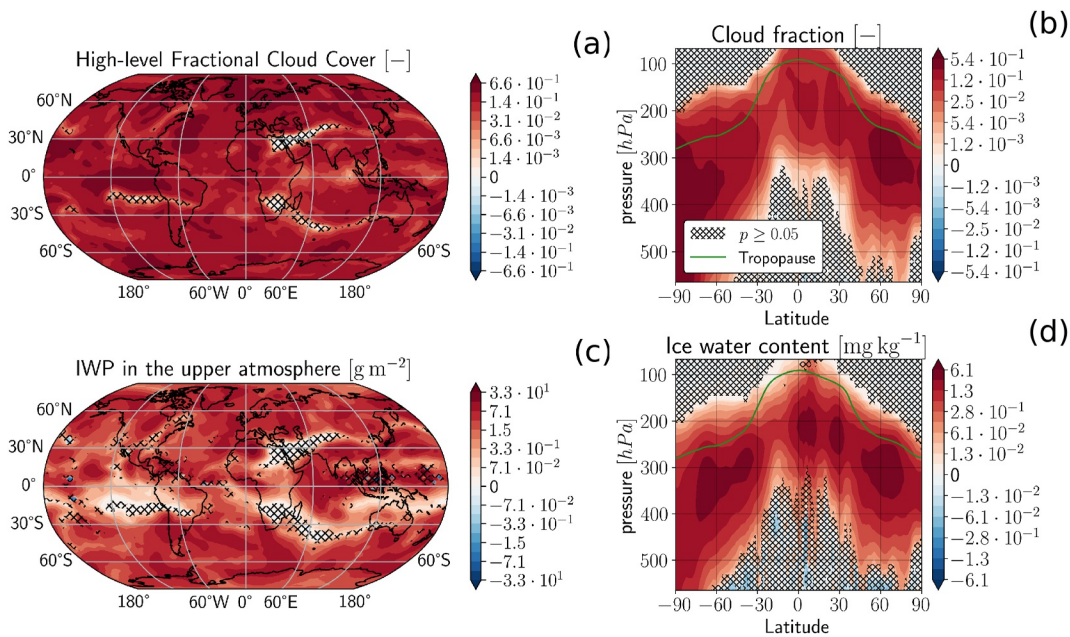

Figure 9. As Figure 6 but for simulations initialized on 11th July.

21698996, 2026, 8, Downloaded from https://agupubs.onlinelibrary.wiley.com/doi/10.1029/2025JD046235 by NICE, National Institute for Health and Care Excellence, Wiley Online Library on [30/04/2026]. See the Terms and Conditions (https://onlinelibrary.wiley.com/terms-and-conditions) on Wiley Online Library for rules of use; OA articles are governed by the applicable Creative Commons License

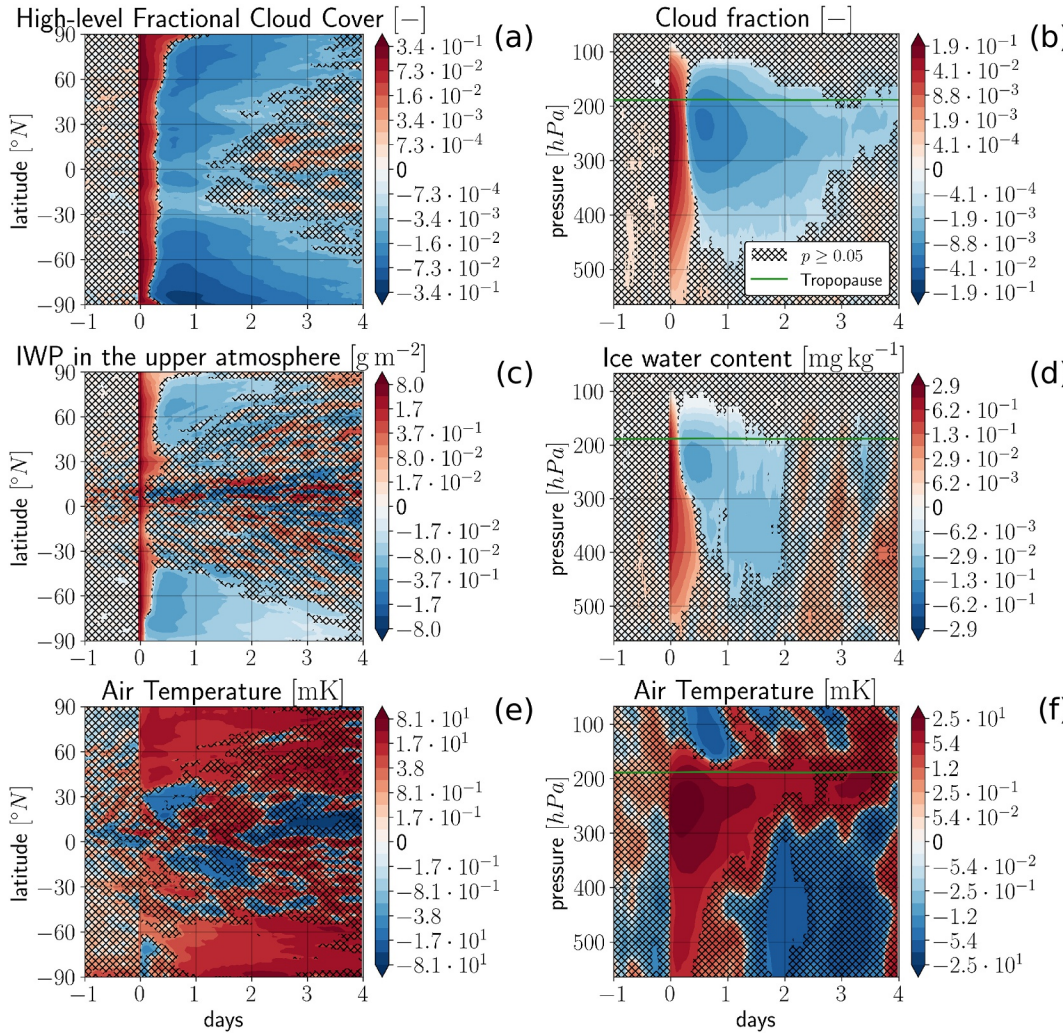

Figure 10. As Figure 7 but for simulations initialized on 11th July.

followed by a decrease relative to the control simulation, which lasts up to 2 days in northern mid-latitudes. Close to the poles, the relative drops in high-level fractional cloud cover persist up to 4 days, as shown in Figure 10a. Overall, no major differences with January simulations are seen in Figures 10a and 10c. The air temperature response is 1.6 time greater in magnitude in northern mid-latitudes below the tropopause level in Figure 10f compared to Figure 7f. The temperature increase persists for twice longer in Norther mid-latitudes in July compared to January (Figure 10f). An air temperature decrease appears during one day after the perturbation around 25°N in Figure 10e. An air temperature decrease of similar magnitude is seen around 25°S in Figure 7e.

Figure 11a shows that ice crystals formed at the tropopause sublimate around 350 hPa in the northern mid-latitudes. By contrast, the positive RHi anomaly in Figure 11c does not extend to such high altitudes and remains comparatively weak in magnitude. The drop in specific humidity reaches lower altitude with time, up to 500 hPa after more than a day. This, again, is interpreted as the sign of ice-crystal sedimentation. In general, the drop in specific humidity and RH_i goes down to 450 hPa in Figures 11a and 11c and it lasts up to 4 days in latitudes close to the poles. Figure 11b shows an increase of supersaturated cloud-free fraction after less than a day around 75°S, similarly to Figure 8b which shows the same pattern at 70°N. The RH_i decrease after the perturbation is the strongest in the South Hemisphere in Figure 11d where the zonal average of RH_i is decreased by −39% (absolute) in the Northern polar latitudes. In comparison, a decrease of the same magnitude is seen in Figure 8d at 60°N.

21698996, 2026, 8, Downloaded from https://agupubs.onlinelibrary.wiley.com/doi/10.1029/2025JD046235 by NICE, National Institute for Health and Care Excellence, Wiley Online Library on [30/04/2026]. See the Terms and Conditions (https://onlinelibrary.wiley.com/terms-and-conditions) on Wiley Online Library for rules of use; OA articles are governed by the applicable Creative Commons License

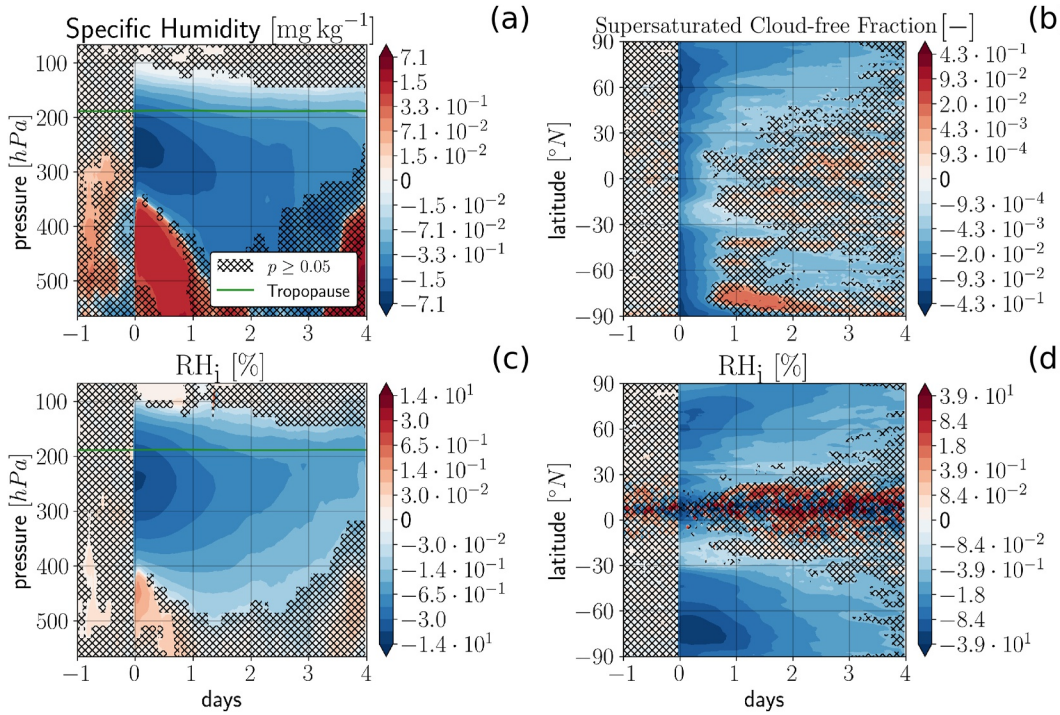

Figure 11. As Figure 8 but for simulations initialized on 11th July.

4.3. Geographical Distribution of the Perturbation

In this section, we discuss the impact of the geographical distribution of the perturbation on the instantaneous RF and the atmospheric adjustments. Different formation mechanisms might give rise to different adjustment strengths. For instance, natural cirrus formation mechanisms are different in the tropical and extra-tropical regions (Heymsfield et al., 2017). In what follows, we use the same setup described in Section 3.1, but the ISSR perturbation is confined to northern mid-latitudes ("Locally perturbed" in Table 2). The number of simulation pairs in the ensemble is $N = 50$.

We compare the globally averaged anomalies of the northern mid-latitude conversion to the results from the global conversion. We hypothesize that the strength of the adjustments is independent on the region where the perturbation is applied. If the response does not depend on the geographical distribution of the initial perturbation, then both anomalies should be proportional to the fraction of global surface area that is within northern mid-latitudes, namely $f_S := (\sin(\pi/3) - \sin(\pi/6))/2 \approx 0.18$.

The instantaneous LW and SW RF at TOA are reported in Table 3. The perturbation restricted to northern mid-latitudes produces larger instantaneous LW RF than the global perturbation multiplied by the surface factor. That is not the case for SW instantaneous RF where the values are equal within variability intervals. In general, the uncertainty on the SW radiative effects is larger than the one on the LW radiative effects, causing major issue

Table 3
Instantaneous RF for Northern Mid-Latitudes Perturbation in the Second Column and Globally Perturbed Simulation in the Third Column, With One Standard Deviation Uncertainty Range

Instantaneous RF [W/m^2]	[30°N, 60°N]	[90°S, 90°N]	$f_S \times$ [90°S, 90°N]
Down. net LW	2.00 ± 0.14	9.72 ± 0.26	1.78 ± 0.05
Down. net SW	−0.51 ± 0.22	−3.27 ± 0.47	−0.60 ± 0.09
Down. net LW + SW	1.49 ± 0.26	6.45 ± 0.65	1.18 ± 0.10

Note. The fourth column corresponds to the third one multiply by the surface factor $f_S \approx 0.18$ (see main text for details). Data extracted from an ensemble of $N = 50$ simulation pairs initialized on 11th January.

21698996, 2026, 8, Downloaded from https://agupubs.onlinelibrary.wiley.com/doi/10.1029/2025JD046235 by NICE, National Institute for Health and Care Excellence, Wiley Online Library on [30/04/2026]. See the Terms and Conditions (https://onlinelibrary.wiley.com/terms-and-conditions) on Wiley Online Library for rules of use; OA articles are governed by the applicable Creative Commons License

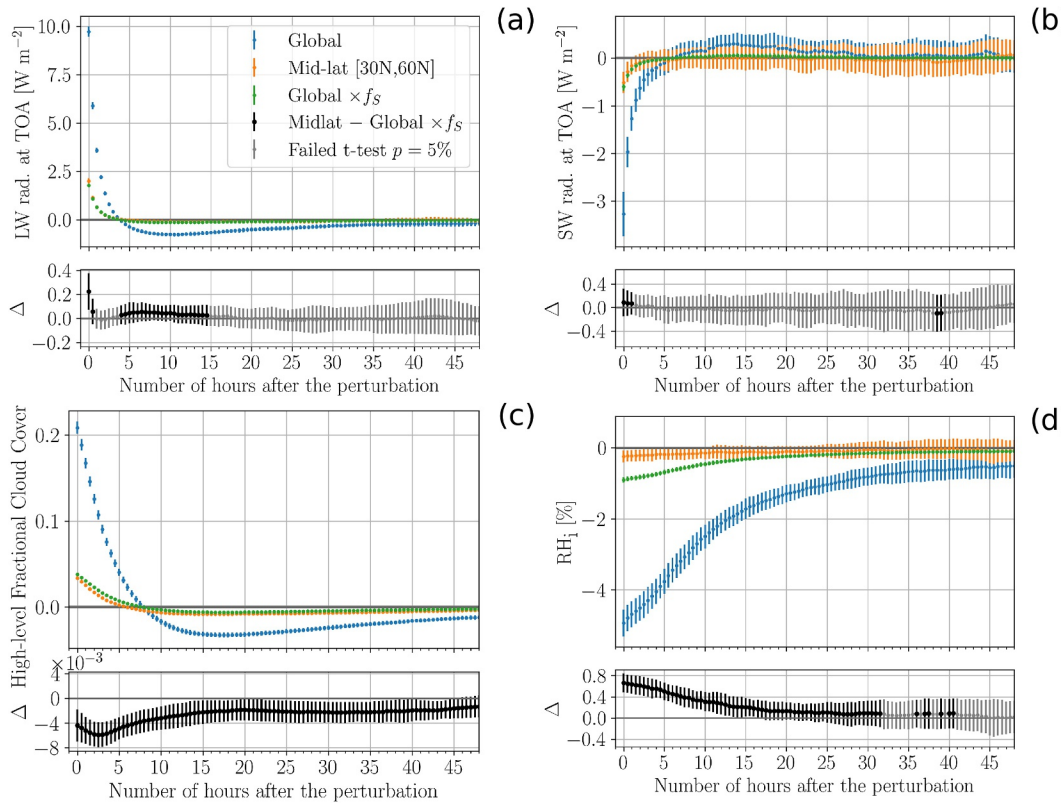

Figure 12. Comparison between a global ISSR conversion (blue) and a conversion restricted to northern mid-latitudes (orange). In green, we plot the anomalies from the global conversion multiplied by the surface factor $f_S \approx 0.18$ (see the main text for details). The bottom part of the panels shows the difference between the orange and the green curves with the error bars showing the ±1 standard deviation interval computed over the $N = 50$ simulation pairs of the ensemble. Data points that do not pass the two-tailed t-test at 5% level are in gray, while significant differences are in black. (a) Downward net LW radiation, in W m^{-2}, at TOA, (b) Downward net SW radiation, in W m^{-2}, at TOA, (c) High-level fractional cloud cover (d) RH$_i$, in %, at the tropopause level. Data are extracted from an ensemble of $N = 50$ simulation pairs initialized on 11th January.

when studying weaker perturbations because the signal becomes smaller than the noise. The difference between total net LW + SW RF is proportionally larger when the perturbation is restricted to Northern mid-latitudes. The difference between the first and the third column in Table 3 is clearly finite as it amounts to 0.31 (0.23, 0.39) where the 95% confidence interval is calculated by a two-tailed t-test. The total instantaneous RF is thus incompatible with the geographically independent hypothesis.

Figure 12 shows how anomalies compare over 2 days after the perturbation. From the second timestep onward, both SW and LW radiation anomalies from the northern mid-latitude conversion and those from global conversion are proportional to the surface factor f_S, as shown in Figures 12a and 12b. This is also the case for other model variables such as the supersaturated cloud-free fraction and the upper-atmospheric IWP.

In contrast, we report two model variables for which the response is not proportional to the surface factor f_S in the first hours after the pulse in Figures 12c and 12d. High-level fractional cloud cover anomaly is slightly larger in the global perturbation, but it remains smaller than a percent difference. Unlike the LW radiative anomaly, the high-level fractional cloud cover anomaly changes sign two hours later in the global perturbation simulation compared to the northern mid-latitude simulations. Conversely the drop in RH$_i$ is stronger when performing a global perturbation. This may indicate that the response of the climate system to a global perturbation is dominated by the response of the tropical deep convection, overwhelming smaller extra-tropical humidity changes. In addition, as the perturbation occurs ahead of the convective systems at mid-latitudes, the humidity might not mix downward efficiently. A similar argument is presented by Schumann and Mayer (2017) and Bickel et al. (2025) in their discussion of heat transfer associated with contrail formation. Consequently, the average RH$_i$ drop at the tropopause level is larger in the global perturbation case.

21698996, 2026, 8, Downloaded from https://agupubs.onlinelibrary.wiley.com/doi/10.1029/2025JD046235 by NICE, National Institute for Health and Care Excellence, Wiley Online Library on [30/04/2026]. See the Terms and Conditions (https://onlinelibrary.wiley.com/terms-and-conditions) on Wiley Online Library for rules of use; OA articles are governed by the applicable Creative Commons License

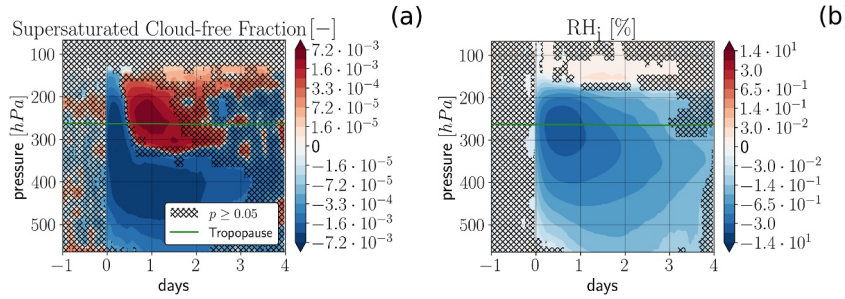

Figure 13. Effect of northern mid-latitude ISSR conversion in the North Hemisphere polar region, [60°N, 90°N]. Time evolution of (a) ice supersaturated cloud-free fraction and (b) RH_i, in %, anomaly vertical profiles. Data extracted from an ensemble of $N = 50$ simulation pairs initialized on 11th January. Regions that do not pass a two-tailed Student's t-test at 5% level are indicated with hatching. Note the logarithmic scale on the color bar. Thus, relatively small anomalies may be statistically significant.

Interestingly, the idealized perturbation of ISSR restricted to northern mid-latitudes is of the same order of magnitude as the results of a recent model study by Bickel et al. (2020) where the forecast air traffic density for 2050 is enhanced by a factor 12. The partitioning between LW and SW differs from that of Bickel et al. (2020): the SW radiative perturbation is weaker, but compatible within one standard deviation, $\left((-0.51 \pm 0.22)\,\mathrm{W\,m^{-2}}\right.$ versus $\left.-0.65\,\mathrm{W\,m^{-2}}\right)$, while the LW perturbation is stronger $\left((2.00 \pm 0.14)\,\mathrm{W\,m^{-2}}\right.$ versus $\left.1.35\,\mathrm{W\,m^{-2}}\right)$. This discrepancy originates from both the fact that the two perturbations are not equally strong but also from radiative uncertainties (Myhre et al., 2009) that may change the degree of compensation between SW an LW.

Nevertheless, our experiment differs from a sustained formation of contrails applied by Bickel et al. (2020). A sustained RF can be viewed as a series of pulses performed at each physical timestep. The consequence is that the perturbation is superimposed onto the adjustments, which may limit the intensity of the forcing and/or the adjustments, possibly in a non-linear way, which limits the usefulness of comparing the calculated RFs. In addition, the parametrizations of sedimentation in both models are different. In our case, sedimentation is dictated by the ice water content only, which means that a large value of IWP leads to a large sedimentation. In the model used by Bickel et al. (2020), the ice crystal number concentration scales with the ice water content when the contrail is formed, such that the mass of each crystal is similar for any given value of IWP. The sedimentation is therefore only slightly impacted by a large value of IWP.

In the northern mid-latitude configuration described above, the effects of the perturbation are not confined between 30°N and 60°N. Figure 13 presents the time-evolution of two anomalies in the North Hemisphere polar region, [60°N, 90°N], outside of the initially perturbed region. Figure 13 shows that supersaturated cloud-free fraction drops by less than a percent (absolute) right after the perturbation. After 6 hours, the anomaly changes sign around the tropopause level and reaches less than a percent absolute increase. It is interesting and somewhat counterintuitive to note that in the polar regions the anomaly in supersaturated cloud-free fraction turns positive after half a day above 300 hPa while the specific humidity anomaly remains negative. This behavior is also seen in Figures 8b and 11b. This may be due to the fact the negative anomaly in cirrus cloud propagates to the polar regions. In the absence of homogeneous freezing, there is thus less condensation of supersaturated water vapor, which lengthens the lifetime of ISSR and therefore their fractional coverage. In Figure 13b, we see that the RH_i reduction reaches -5% at the tropopause level after two hours. Then, the RH_i anomaly is exponentially suppressed, like in other regions.

4.4. Linearity of the Adjustments to the Initial RF

In this part, we study how the adjustments change with the size of the ISSR humidity conversion. To do so, instead of performing a total conversion of the ISSR water vapor into cirrus clouds, we only convert a fraction $f \in [0, 1]$ of the ISSR water vapor (11) thus becomes

$$q_{\mathrm{cld}} := q_{\mathrm{cld}} + f\, q_{\mathrm{issr}}\,. \tag{18}$$

21698996, 2026, 8, Downloaded from https://agupubs.onlinelibrary.wiley.com/doi/10.1029/2025JD046235 by NICE, National Institute for Health and Care Excellence, Wiley Online Library on [30/04/2026]. See the Terms and Conditions (https://onlinelibrary.wiley.com/terms-and-conditions) on Wiley Online Library for rules of use; OA articles are governed by the applicable Creative Commons License

Table 4
Instantaneous RF for Different Values of the Fraction f of ISSR Water Vapor That is Converted Into Cirrus Cloud With One Standard Deviation Uncertainty Range

f	Radiative perturbation	Instantaneous RF $[\mathrm{W\,m^{-2}}]$	Normalized RF $[\mathrm{W\,m^{-2}}]$
1.0	LW	9.72 ± 0.26	9.72 ± 0.26
	SW	−3.27 ± 0.47	−3.27 ± 0.47
0.5	LW	5.09 ± 0.17	10.2 ± 0.34
	SW	−1.69 ± 0.26	−3.38 ± 0.52
0.1	LW	1.08 ± 0.06	10.8 ± 0.60
	SW	−0.35 ± 0.19	−3.50 ± 1.90
0.05	LW	0.54 ± 0.07	10.8 ± 1.40
	SW	−0.16 ± 0.17	−3.20 ± 3.40
0.01	LW	0.11 ± 0.07	11.0 ± 7.00
	SW	−0.06 ± 0.16	−6.00 ± 16.0

Note. Data extracted from an ensemble of $N = 50$ simulation pairs for $f = 1.0$, 0.5, and 0.1, from $N = 150$ for $f = 0.05$, and from $N = 100$ for $f = 0.01$. The third column reports the instantaneous RF and the last column the value normalized by the intensity of perturbation f. Simulation are initialized on 11th January.

The other equations are modified accordingly to ensure the conservation of total water. The supersaturated cloud-free fraction χ_{issr} is reduced by same fraction f. The case $f = 1$ corresponds to the results presented in the previous sections. Each value of f is associated with a set of anomalies labeled $y_f(t)$. The number of experiments needed to achieve statistical significance increases with a decreasing value of f, because smaller perturbations are more difficult to extract from internal variability.

We report instantaneous RF values in Table 4. If instantaneous RF is linear with the intensity of the ISSR perturbation, then it should scale with the factor f. For $f = 0.5$ and $f = 0.1$, the LW instantaneous RF exhibits sublinear behavior, whereas the SW instantaneous RF remains linear. For smaller values of f, both LW and SW instantaneous RF appear linear; however, it is difficult to determine whether this reflects true linearity or is instead a consequence of larger uncertainties. Unlike Bickel et al. (2020), we do not see a saturation of the instantaneous RF because the type of perturbation differs. In Bickel et al. (2020), cirrus cloud formation is prescribed at the locations of air traffic. If the air traffic density is finite, contrails can be persist when formed in ISSRs, consuming at least partly the local available humidty. At some point, increasing the traffic cannot create additional contrails because humidity does not have time to be restored. In this study, we do not have such a strong saturation effect as we directly convert on an unperturbed climate system the maximal amount of available ISSR humidity into ice crystal ($f = 1$) and compare to a fraction of it ($f \neq 1$).

In Figure 14, we compare the evolution of several anomalies over a period of one day after the perturbation by plotting the difference between normalized anomalies, $f \neq 1$, and the reference case, $f = 1$. Namely,

$$y_f(t)/f - y_1(t). \tag{19}$$

If the adjustments are linear with respect to the factor f, then the differences should remain around zero. Figure 14 shows that radiative anomalies are mostly linear with the intensity of the initial perturbation. The LW and net SW + LW anomalies display a linear behavior from the second timestep onward. On the other hand, the high-level fractional cloud cover is strongly non-linear. It reveals that the cloud cover anomaly is proportionally larger for smaller perturbation intensity. This behavior is the sign of a saturation effect: when only a fraction of the ISSRs is converted into cirrus clouds, the remaining supersaturated cloud-free fraction acts as source of available humidity for further ice crystal nucleation. Additional model variables are analyzed in Figure S3 of Supporting Information S1.

21698996, 2026, 8, Downloaded from https://agupubs.onlinelibrary.wiley.com/doi/10.1029/2025JD046235 by NICE, National Institute for Health and Care Excellence, Wiley Online Library on [30/04/2026]. See the Terms and Conditions (https://onlinelibrary.wiley.com/terms-and-conditions) on Wiley Online Library for rules of use; OA articles are governed by the applicable Creative Commons License

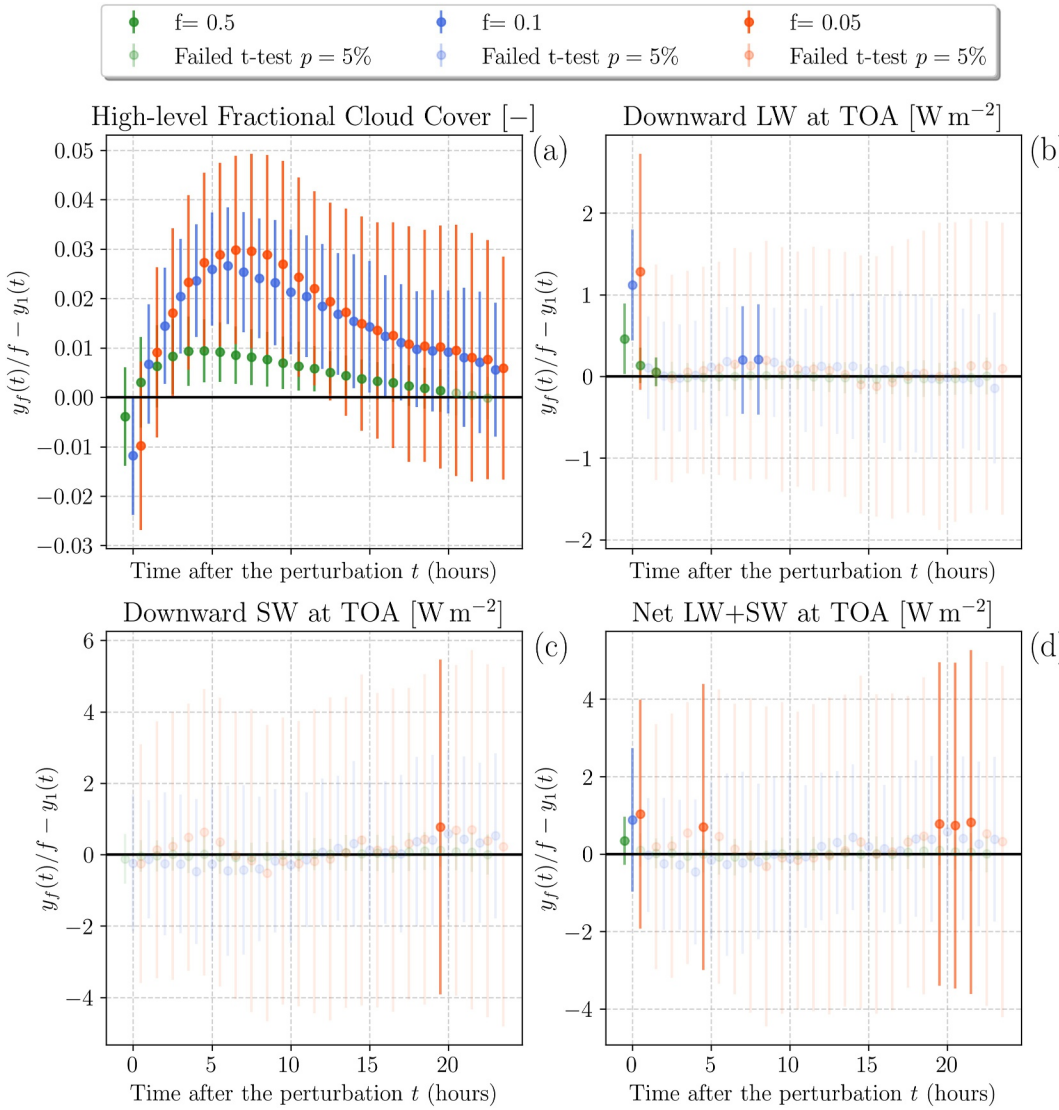

Figure 14. Difference between normalized anomalies of (a) high-level fractional cloud cover, (b) Downward LW, (c) Downward SW, and (d) net SW + LW radiative fluxes at TOA for different fractions of ISSRs converted into clouds, $f = 0.5$ in green, $f = 0.1$ in blue, and $f = 0.05$ in orange, and the reference case, $f = 1$ according to (19). Error envelopes indicate the ±1 standard deviation interval computed among simulation pair ensembles. Data are extracted from an ensemble of $N = 50$ simulation pairs initialized on 11th January, except for $f = 0.05$ where $N = 150$ to further reduce the statistical impact of atmospheric variability. The time resolution of the x-axis is 1 hour, down form 30 min in the simulations. Compatibility with the reference case is checked using a two-tailed t-test at 5% level.

5. Conclusion

This study identifies and quantifies atmospheric adjustments to in situ cirrus cloud formation, which is relevant to the study of the climate impact of aviation contrails and CCT methods. Atmospheric adjustments are responses to an RF that evolve without a corresponding change in GSAT. Quantifying adjustments is important because they are potentially associated with a large radiative response that may weaken or amplify the initial RF. Unfortunately, this quantification is difficult because adjustments can be masked by internal variability of the atmosphere and are superimposed with other types of responses.

We have presented a statistically robust framework to investigate atmospheric adjustments triggered by a pulse perturbation, using an ensemble of 50 pairs of 10-day simulations with ICOLMDZ whose atmospheric model incorporates a new parametrization of ice supersaturation. The pulse consists of an instantaneous conversion of

21698996, 2026, 8, Downloaded from https://agupubs.onlinelibrary.wiley.com/doi/10.1029/2025JD046235 by NICE, National Institute for Health and Care Excellence, Wiley Online Library on [30/04/2026]. See the Terms and Conditions (https://onlinelibrary.wiley.com/terms-and-conditions) on Wiley Online Library for rules of use; OA articles are governed by the applicable Creative Commons License

21698996, 2026, 8, Downloaded from https://agupubs.onlinelibrary.wiley.com/doi/10.1029/2025JD046235 by NICE, National Institute for Health and Care Excellence, Wiley Online Library on [30/04/2026]. See the Terms and Conditions (https://onlinelibrary.wiley.com/terms-and-conditions) on Wiley Online Library for rules of use; OA articles are governed by the applicable Creative Commons License

ISSRs into cirrus clouds, applied at eight different times of day on 11th January or 11th July. The cirrus formation pulse modifies the distribution of specific humidity in the upper atmosphere, thereby influencing subsequent cloud formation as humidity gradually rebuilds toward unperturbed values. By adopting a pulse perturbation rather than a sustained perturbation, our approach enables a clean attribution of the temporal evolution of atmospheric adjustments.

ICOLMDZ, the climate model used in this study, shows a local, cold bias of up to 3 K at 200 hPa, which reduces the saturation pressure by 30%, affecting the ISSR distribution. Bias correction is often done by applying nudging, but studying adjustments precludes the use of standard nudging procedures, as the adjustment mechanisms would be suppressed by Newtonian relaxation. To avoid this suppression, we implemented an online bias correction technique, called soft nudging, to reduce the ICOLMDZ cold temperature bias compared to the ERA5 reanalysis.

The initial increase in high-level fractional cloud cover following the perturbation reaches up to 66% locally in January. The IWP in the upper atmosphere is increased locally by up to 33 g m^{-2}, leading to a strong greenhouse effect and larger cloud albedo. Then, the sedimentation and sublimation of ice crystals further drive humidity redistribution, as evidenced by the decrease in specific humidity and the associated RH_i decrease modeled in both January and July. The radiative effects of the perturbation are exponentially attenuated within a couple of hours after the perturbation. In our simulations, adjustments are strong enough to revert the sign of the initial RF. The perturbation exerts a LW RF that is initially positive, but is counteracted by negative adjustments. Conversely, the initial SW RF is negative, but is counteracted by positive adjustments. The net SW + LW RF therefore exhibits a complex temporal behavior, which will be further characterized in future work.

The analysis of RH_i anomaly has showed that the formation of cirrus clouds in the model significantly disrupts the ice supersaturation conditions necessary for ISSR maintenance. The negative RH_i anomalies persisting for several days highlight the self-limiting nature of ice cloud formation: the act of forming ice clouds suppresses the environment's ability to sustain them further. The sublimation of sedimented ice crystals at lower altitudes leads to localized increases in water vapor and capture of latent heat, causing very small but statistically significant temperature decreases of the order of tens of millikelvins. Meanwhile, the enhanced cloud cover at the tropopause modifies radiative fluxes, cooling the air above the tropopause and warming it below.

We have assessed whether the atmospheric response is geographically uniform, that is, whether the normalized response is independent of the spatial extent of the imposed perturbation when applied either globally or confined to the northern mid-latitudes [30°N, 60°N]. We have found that the SW radiative response is largely invariant to the location of the perturbation. Within the limited set of regions considered here, the instantaneous LW and LW + SW RFs are proportionally stronger when the perturbation excludes the tropics; however, from the second model timestep onward, the radiative response becomes effectively independent of perturbation geography. In contrast, adjustments in high-level fractional cloud cover and upper-tropospheric RH_i exhibit pronounced geographic sensitivity, indicating that the tropics exert a dominant control on the overall atmospheric response when included in the initial perturbation. While the applied perturbation is idealized, we show that the RF in our experiment restricted to northern mid-latitudes is close to that computed in a recent study with air traffic density for the year 2050 scaled up to 12 times (Bickel et al., 2020). It may indicate that a sufficiently strong amplification of air traffic may locally consume most of the available ISSR by converting it into cirrus clouds, thereby approximating the mechanism represented in our pulse perturbation. Under such conditions, the resulting local adjustments could resemble, in magnitude and behavior, the global adjustments identified in our idealized experiment.

Our method allows for smaller perturbations by varying the fraction of supersaturated cloud-free fraction converted into cirrus clouds. We have assessed the linearity of the atmospheric response by perturbing a fraction f of the ISSR humidity. Most model variables present a linear behavior with respect to f over the range of perturbation amplitudes considered. However, the instantaneous LW and net LW + SW RFs exhibit a weak, but statistically significant, tendency toward sublinear behavior: although the deviations are small in magnitude, the proportional response appears slightly reduced for the largest perturbations ($f = 1.0$ and 0.5) relative to the smaller ones ($f = 0.1$, 0.05, and 0.01). Statistical significance could be further improved by increasing the number of simulation pairs in the ensemble for $f = 0.05$ and $f = 0.01$. From the second model timestep onward, the LW and net SW + LW radiative response becomes effectively linear. In contrast, the high-level cloud fraction exhibits a pronounced non-linear response: within a few hours of the perturbation, small values of f lead to

disproportionately large increases in cloud cover. The LW response appears nearly linear because cloud optical thickness decreases rapidly, which constrains any additional radiative impact at larger perturbation amplitudes.

Future work will aim to assess the feedbacks in atmosphere-ocean coupled climate simulations and to estimate the GSAT change by implementing a contrail formation and evolution parametrization in ICOLMDZ. The ensemble method is also expected to reduce atmospheric variability, thereby limiting the required scaling of air traffic density. In addition, radiative adjustments could be investigated under more realistic scenarios, accounting for synoptic meteorological conditions and the geographical and temporal variability of air traffic.

Conflict of Interest

The authors declare no conflicts of interest relevant to this study.

Availability Statement

Software—The custom version of ICOLMDZ used in this study is based on the *svn* release 5437, which can be downloaded and installed on a Linux computer by running the `install_lmdz.sh` script available at: https://web.lmd.jussieu.fr/~lmdz/pub/install_lmdz.sh. We switch on the conversion of ISSRs into clouds in the `lscp_condensation` subroutine.

Data—Processed data and scripts that have been used to generate simulation pairs with ICOLMDZ and to produce the plots of this study are publicly available (Juvin-Quarroz, 2026).

Acknowledgments

We deeply thank the Reviewers for their thorough reading of the manuscript, which greatly enhanced the clarity, readability, robustness, and consistency of the presentation of the results. This research has been supported by the French Ministère de la Transition Écologique et Solidaire under the Climaviation project (Grant DGAC N2021-39), with support from France's Plan National de Relance et de Résilience (PNRR) and the European Union's NextGenerationEU. This study benefited from the IPSL mesocenter ESPRI facility which is supported by CNRS, Sorbonne Université, Labex L-IPSL, CNES and École Polytechnique. The ICOLMDZ experiments were performed using the HPC resources of TGCC under the allocation gencmip6 as provided by GENCI (Grand Equipement National de Calcul Intensif). This project has received funding from the European Research Council (ERC) under the European Union's Horizon 2020 research and innovation programme (Grant 951596) through the AWACA project. Open access publication funding provided by COUPERIN CY26.

References

Baumgartner, M., Weigel, R., Harvey, A. H., Plöger, F., Achatz, U., & Spichtinger, P. (2020). Reappraising the appropriate calculation of a common meteorological quantity: Potential temperature. *Atmospheric Chemistry and Physics*, *20*(24), 15585–15616. https://doi.org/10.5194/acp-20-15585-2020

Bickel, M., Ponater, M., Bock, L., Burkhardt, U., & Reineke, S. (2020). Estimating the effective radiative forcing of contrail cirrus. *Journal of Climate*, *33*(5), 1991–2005. https://doi.org/10.1175/jcli-d-19-0467.1

Bickel, M., Ponater, M., Burkhardt, U., Righi, M., Hendricks, J., & Jöckel, P. (2025). Contrail cirrus climate impact: From radiative forcing to surface temperature change. *Journal of Climate*, *38*(8), 1895–1912. https://doi.org/10.1175/jcli-d-24-0245.1

Borella, A., Vignon, E., Boucher, O., Meurdesoif, Y., & Fairhead, L. (2025). A new prognostic parameterization of subgrid ice supersaturation and cirrus clouds in the ICOLMDZ AGCM. *Journal of Advances in Modeling Earth Systems*, *17*(8), e2024MS004918. https://doi.org/10.1029/2024ms004918

Boucher, O. (1999). Air traffic may increase cirrus cloudiness. *Nature*, *397*(6714), 30–31. https://doi.org/10.1038/16169

Boucher, O., Randall, D., Artaxo, P., Bretherton, C., Feingold, G., Forster, P., et al. (Eds.), Climate change 2013: The physical science basis. Contribution of working group I to the fifth assessment report of the Intergovernmental Panel on climate Change. Cambridge, United Kingdom and New York, NY, USA: Cambridge University Press.

Boucher, O., Servonnat, J., Albright, A. L., Aumont, O., Balkanski, Y., Bastrikov, V., et al. (2020). Presentation and evaluation of the IPSL-CM6A-LR climate model. *Journal of Advances in Modeling Earth Systems*, *12*(7), e2019MS002010. https://doi.org/10.1029/2019ms002010

Ceppi, P., Brient, F., Zelinka, M. D., & Hartmann, D. L. (2017). Cloud feedback mechanisms and their representation in global climate models. *WIREs Climate Change*, *8*(4), e465. https://doi.org/10.1002/wcc.465

Chen, T., Rossow, W. B., & Zhang, Y. (2000). Radiative effects of cloud-type variations. *Journal of Climate*, *13*(1). https://doi.org/10.1175/1520-0442(2000)013⟨0264:reoctv⟩2.0.co;2

Chepfer, H., Bony, S., Winker, D., Cesana, G., Dufresne, J. L., Minnis, P., et al. (2010). The GCM-oriented CALIPSO cloud product (CALIPSO-GOCCP). *Journal of Geophysical Research*, *115*(D4). https://doi.org/10.1029/2009jd012251

Dannet, G., Boucher, O., & Bellouin, N. (2024). Features and evolution of civil aviation CO2 emissions based on ADS-B data for the period between 2019–2024. *Metascience in Aerospace*, *1*(4), 346–370. https://doi.org/10.3934/mina.2024016

Dubos, T., Dubey, S., Tort, M., Mittal, R., Meurdesoif, Y., & Hourdin, F. (2015). DYNAMICO-1.0, an icosahedral hydrostatic dynamical core designed for consistency and versatility. *Geoscientific Model Development*, *8*(10), 3131–3150. https://doi.org/10.5194/gmd-8-3131-2015

Duda, D. P., Bedka, S. T., Minnis, P., Spangenberg, D., Khlopenkov, K., Chee, T., & Smith, W. L., Jr. (2019). Northern hemisphere contrail properties derived from terra and aqua MODIS data for 2006 and 2012. *Atmospheric Chemistry and Physics*, *19*(8), 5313–5330. https://doi.org/10.5194/acp-19-5313-2019

Forster, P. M., Storelvmo, T., Armour, K., Collins, W., Dufresne, J.-L., Frame, D., et al. (Eds.), Climate change 2021: The physical science basis. Contribution of working group I to the sixth assessment report of the Intergovernmental Panel on climate Change (pp. 923–1054). Cambridge, United Kingdom and New York, NY, USA: Cambridge University Press. https://doi.org/10.1017/9781009157896.009

Fouquart, Y., & Bonnel, B. (1980). Computations of solar heating of the Earth's atmosphere—A new parameterization. *Beiträge zur Physik der Atmosphäre*, *53*, 35–62.

Gasparini, B., & Lohmann, U. (2016). Why cirrus cloud seeding cannot substantially cool the planet. *Journal of Geophysical Research: Atmospheres*, *121*(9), 4877–4893. https://doi.org/10.1002/2015jd024666

Gasparini, B., McGraw, Z., Storelvmo, T., & Lohmann, U. (2020). To what extent can cirrus cloud seeding counteract global warming? *Environmental Research Letters*, *15*(5), 054002. https://doi.org/10.1088/1748-9326/ab71a3

Gasparini, B., Münch, S., Poncet, L., Feldmann, M., & Lohmann, U. (2017). Is increasing ice crystal sedimentation velocity in geoengineering simulations a good proxy for cirrus cloud seeding? *Atmospheric Chemistry and Physics*, *17*(7), 4871–4885. https://doi.org/10.5194/acp-17-4871-2017

21698996, 2026, 8, Downloaded from https://agupubs.onlinelibrary.wiley.com/doi/10.1029/2025JD046235 by NICE, National Institute for Health and Care Excellence, Wiley Online Library on [30/04/2026]. See the Terms and Conditions (https://onlinelibrary.wiley.com/terms-and-conditions) on Wiley Online Library for rules of use; OA articles are governed by the applicable Creative Commons License

Gettelman, A., Hegglin, M. I., Son, S., Kim, J., Fujiwara, M., Birner, T., et al. (2010). Multimodel assessment of the upper troposphere and lower stratosphere: Tropics and global trends. *Journal of Geophysical Research*, *115*(D3). https://doi.org/10.1029/2009jd013638

Gierens, K. (2012). Selected topics on the interaction between cirrus clouds and embedded contrails. *Atmospheric Chemistry and Physics*, *12*(24), 11943–11949. https://doi.org/10.5194/acp-12-11943-2012

Gierens, K., Matthes, S., & Rohs, S. (2020). How well can persistent contrails be predicted? *Aerospace*, *7*(12), 169. https://doi.org/10.3390/aerospace7120169

Hansen, J., Lacis, A., Rind, D., Russell, G., Stone, P., Fung, I., et al. (1984). Climate sensitivity: Analysis of feedback mechanisms. In J. E. Hansen & T. Takahashi (Eds.), *Climate processes and climate sensitivity* (pp. 130–163). Washington, D.C.: American Geophysical Union.

Hansen, J., Sato, M., Ruedy, R., Nazarenko, L., Lacis, A., Schmidt, G. A., et al. (2005). Efficacy of climate forcings. *Journal of Geophysical Research*, *110*(D18). https://doi.org/10.1029/2005jd005776

Hersbach, H., Bell, B., Berrisford, P., Hirahara, S., Horányi, A., Muñoz-Sabater, J., et al. (2020). The ERA5 global reanalysis. *Quarterly Journal of the Royal Meteorological Society*, *146*(730), 1999–2049. https://doi.org/10.1002/qj.3803

Heymsfield, A. J., & Donner, L. J. (1990). A scheme for parameterizing ice-cloud water content in general circulation models. *Journal of the Atmospheric Sciences*, *47*(15), 1865–1877. https://doi.org/10.1175/1520-0469(1990)047⟨1865:asfpic⟩2.0.co;2

Heymsfield, A. J., Krämer, M., Luebke, A., Brown, P., Cziczo, D. J., Franklin, C., et al. (2017). Cirrus clouds. *Meteorological Monographs*, *58*, 2.1–2.26. https://doi.org/10.1175/amsmonographs-d-16-0010.1

Hong, Y., & Liu, G. (2015). The characteristics of ice cloud properties derived from cloudsat and CALIPSO measurements. *Journal of Climate*, *28*(9), 3880–3901. https://doi.org/10.1175/jcli-d-14-00666.1

Hourdin, F., Rio, C., Grandpeix, J., Madeleine, J., Cheruy, F., Rochetin, N., et al. (2020). LMDZ6A: The atmospheric component of the IPSL climate model with improved and better tuned physics. *Journal of Advances in Modeling Earth Systems*, *12*(7), e2019MS001892. https://doi.org/10.1029/2019ms001892

Jeuken, A. B. M., Siegmund, P. C., Heijboer, L. C., Feichter, J., & Bengtsson, L. (1996). On the potential of assimilating meteorological analyses in a global climate model for the purpose of model validation. *Journal of Geophysical Research*, *101*(D12), 16939–16950. https://doi.org/10.1029/96jd01218

Juvin-Quarroz, J. (2026). Scripts to generate ensembles of simulation pairs using ICOLMDZ [Dataset]. *Zenodo*. https://doi.org/10.5281/ZENODO.18873672

Kärcher, B. (2017). Cirrus clouds and their response to anthropogenic activities. *Current Climate Change Reports*, *3*(1), 45–57. https://doi.org/10.1007/s40641-017-0060-3

Kärcher, B. (2018). Formation and radiative forcing of contrail cirrus. *Nature Communications*, *9*(1), 1824. https://doi.org/10.1038/s41467-018-04068-0

Kärcher, B., & Corcos, M. (2025). On the lifetimes of persistent contrails and contrail cirrus. *Journal of Geophysical Research: Atmospheres*, *130*(20), e2025JD044488. https://doi.org/10.1029/2025jd044488

Kharin, V. V., & Scinocca, J. F. (2012). The impact of model fidelity on seasonal predictive skill. *Geophysical Research Letters*, *39*(18). https://doi.org/10.1029/2012gl052815

Koop, T., Luo, B., Tsias, A., & Peter, T. (2000). Water activity as the determinant for homogeneous ice nucleation in aqueous solutions. *Nature*, *406*(6796), 611–614. https://doi.org/10.1038/35020537

Krinner, G., Kharin, V., Roehrig, R., Scinocca, J., & Codron, F. (2020). Historically-based run-time bias corrections substantially improve model projections of 100 years of future climate change. *Communications Earth & Environment*, *1*(1), 29. https://doi.org/10.1038/s43247-020-00035-0

Lamquin, N., Stubenrauch, C. J., Gierens, K., Burkhardt, U., & Smit, H. (2012). A global climatology of upper-tropospheric ice supersaturation occurrence inferred from the atmospheric infrared sounder calibrated by MOZAIC. *Atmospheric Chemistry and Physics*, *12*(1), 381–405. https://doi.org/10.5194/acp-12-381-2012

Lee, D. S., Fahey, D., Skowron, A., Allen, M., Burkhardt, U., Chen, Q., et al. (2021). The contribution of global aviation to anthropogenic climate forcing for 2000 to 2018. *Atmospheric Environment*, *244*, 117834. https://doi.org/10.1016/j.atmosenv.2020.117834

Liu, J., & Shi, X. (2021). Estimating the potential cooling effect of cirrus thinning achieved via the seeding approach. *Atmospheric Chemistry and Physics*, *21*(13), 10609–10624. https://doi.org/10.5194/acp-21-10609-2021

Loeb, N. G., Wielicki, B. A., Doelling, D. R., Smith, G. L., Keyes, D. F., Kato, S., et al. (2009). Toward optimal closure of the Earth's top-of-atmosphere radiation budget. *Journal of Climate*, *22*(3), 748–766. https://doi.org/10.1175/2008jcli2637.1

Madeleine, J., Hourdin, F., Grandpeix, J., Rio, C., Dufresne, J., Vignon, E., et al. (2020). Improved representation of clouds in the atmospheric component LMDZ6A of the IPSL-CM6A Earth system model. *Journal of Advances in Modeling Earth Systems*, *12*(10), e2020MS002046. https://doi.org/10.1029/2020ms002046

Marvel, K., Schmidt, G. A., Miller, R. L., & Nazarenko, L. S. (2015). Implications for climate sensitivity from the response to individual forcings. *Nature Climate Change*, *6*(4), 386–389. https://doi.org/10.1038/nclimate2888

Mitchell, D. L., & Finnegan, W. (2009). Modification of cirrus clouds to reduce global warming. *Environmental Research Letters*, *4*(4), 045102. https://doi.org/10.1088/1748-9326/4/4/045102

Mlawer, E. J., Taubman, S. J., Brown, P. D., Iacono, M. J., & Clough, S. A. (1997). Radiative transfer for inhomogeneous atmospheres: RRTM, a validated correlated-k model for the longwave. *Journal of Geophysical Research*, *102*(D14), 16663–16682. https://doi.org/10.1029/97jd00237

Myhre, G., Kvalevåg, M., Rädel, G., Cook, J., Shine, K. P., Clark, H., et al. (2009). Intercomparison of radiative forcing calculations of stratospheric water vapour and contrails. *Meteorologische Zeitschrift*, *18*(6), 585–596. https://doi.org/10.1127/0941-2948/2009/0411

Myhre, G., Shindell, D., Bréon, F.-M., Collins, W., Fuglestvedt, J., Huang, J., et al. (Eds.), Climate change 2013: The physical science basis. Contribution of working group I to the fifth assessment report of the Intergovernmental Panel on climate Change (pp. 659–740). Cambridge, United Kingdom and New York, NY, USA: Cambridge University Press.

Penner, J. E., Zhou, C., & Liu, X. (2015). Can cirrus cloud seeding be used for geoengineering? *Geophysical Research Letters*, *42*(20), 8775–8782. https://doi.org/10.1002/2015gl065992

Petzold, A., Thouret, V., Gerbig, C., Zahn, A., Brenninkmeijer, C. A. M., Gallagher, M., & IAGOS Team. (2015). Global-scale atmosphere monitoring by in-service aircraft—Current achievements and future prospects of the European research infrastructure IAGOS. *Tellus B: Chemical and Physical Meteorology*, *67*(1), 28452. https://doi.org/10.3402/tellusb.v67.28452

Ponater, M., Bickel, M., Bock, L., & Burkhardt, U. (2021). Towards determining the contrail cirrus efficacy. *Aerospace*, *8*(2), 42. https://doi.org/10.3390/aerospace8020042

Ponater, M., Marquart, S., Sausen, R., & Schumann, U. (2005). On contrail climate sensitivity. *Geophysical Research Letters*, *32*(10). https://doi.org/10.1029/2005gl022580

21698996, 2026, 8, Downloaded from https://agupubs.onlinelibrary.wiley.com/doi/10.1029/2025JD046235 by NICE, National Institute for Health and Care Excellence, Wiley Online Library on [30/04/2026]. See the Terms and Conditions (https://onlinelibrary.wiley.com/terms-and-conditions) on Wiley Online Library for rules of use; OA articles are governed by the applicable Creative Commons License

Proske, U., Ferrachat, S., Klampt, S., Abeling, M., & Lohmann, U. (2023). Addressing complexity in global aerosol climate model cloud microphysics. *Journal of Advances in Modeling Earth Systems*, *15*(5), e2022MS003571. https://doi.org/10.1029/2022ms003571

Quaas, J., Andrews, T., Bellouin, N., Block, K., Boucher, O., Ceppi, P., et al. (2024). Adjustments to climate perturbations—mechanisms, implications, observational constraints. *AGU Advances*, *5*(5), e2023AV001144. https://doi.org/10.1029/2023AV001144

Quaas, J., Gryspeerdt, E., Vautard, R., & Boucher, O. (2021). Climate impact of aircraft-induced cirrus assessed from satellite observations before and during COVID-19. *Environmental Research Letters*, *16*(6), 064051. https://doi.org/10.1088/1748-9326/abf686

Rap, A., Forster, P. M., Haywood, J. M., Jones, A., & Boucher, O. (2010). Estimating the climate impact of linear contrails using the UK Met Office climate model. *Geophysical Research Letters*, *37*(20). https://doi.org/10.1029/2010gl045161

Ren, C., & Mackenzie, A. R. (2005). Cirrus parametrization and the role of ice nuclei. *Quarterly Journal of the Royal Meteorological Society*, *131*(608), 1585–1605. https://doi.org/10.1256/qj.04.126

Richardson, T. B., Forster, P. M., Smith, C. J., Maycock, A. C., Wood, T., Andrews, T., et al. (2019). Efficacy of climate forcings in PDRMIP models. *Journal of Geophysical Research: Atmospheres*, *124*(23), 12824–12844. https://doi.org/10.1029/2019jd030581

Rugenstein, M. A. A., Sedláček, J., & Knutti, R. (2016). Nonlinearities in patterns of long-term ocean warming. *Geophysical Research Letters*, *43*(7), 3380–3388. https://doi.org/10.1002/2016gl068041

Sanogo, S., Boucher, O., Bellouin, N., Borella, A., Wolf, K., & Rohs, S. (2024). Variability in the properties of the distribution of the relative humidity with respect to ice: Implications for contrail formation. *Atmospheric Chemistry and Physics*, *24*(9), 5495–5511. https://doi.org/10.5194/acp-24-5495-2024

Schlimme, I., Macke, A., & Reichardt, J. (2005). The impact of ice crystal shapes, size distributions, and spatial structures of cirrus clouds on solar radiative fluxes. *Journal of the Atmospheric Sciences*, *62*(7), 2274–2283. https://doi.org/10.1175/jas3459.1

Schumann, U., & Mayer, B. (2017). Sensitivity of surface temperature to radiative forcing by contrail cirrus in a radiative-mixing model. *Atmospheric Chemistry and Physics*, *17*(22), 13833–13848. https://doi.org/10.5194/acp-17-13833-2017

Schumann, U., & Seifert, A. (2025). On the weather impact of contrails: New insights from coupled ICON–CoCiP simulations. *EGUsphere*, *2025*, 1–43. https://doi.org/10.5194/egusphere-2025-4512

Sherwood, S. C., Bony, S., Boucher, O., Bretherton, C., Forster, P. M., Gregory, J. M., & Stevens, B. (2015). Adjustments in the forcing-feedback framework for understanding climate change. *Bulletin of the American Meteorological Society*, *96*(2), 217–228. https://doi.org/10.1175/bams-d-13-00167.1

Shindell, D., & Faluvegi, G. (2009). Climate response to regional radiative forcing during the twentieth century. *Nature Geoscience*, *2*(4), 294–300. https://doi.org/10.1038/ngeo473

Shine, K. P., Highwood, E. J., Rädel, G., Stuber, N., & Balkanski, Y. (2012). Climate model calculations of the impact of aerosols from road transport and shipping. *Atmospheric and Oceanic Optics*, *25*(1), 62–70. https://doi.org/10.1134/s1024856012010125

Storelvmo, T., & Herger, N. (2014). Cirrus cloud susceptibility to the injection of ice nuclei in the upper troposphere. *Journal of Geophysical Research: Atmospheres*, *119*(5), 2375–2389. https://doi.org/10.1002/2013jd020816

Teoh, R., Engberg, Z., Schumann, U., Voigt, C., Shapiro, M., Rohs, S., & Stettler, M. E. J. (2024). Global aviation contrail climate effects from 2019 to 2021. *Atmospheric Chemistry and Physics*, *24*(10), 6071–6093. https://doi.org/10.5194/acp-24-6071-2024

Tully, C., Neubauer, D., Omanovic, N., & Lohmann, U. (2022). Cirrus cloud thinning using a more physically based ice microphysics scheme in the ECHAM-HAM general circulation model. *Atmospheric Chemistry and Physics*, *22*(17), 11455–11484. https://doi.org/10.5194/acp-22-11455-2022

Wilson Kemsley, S., Nowack, P., & Ceppi, P. (2025). Climate models underestimate global decreases in high-cloud amount with warming. *Geophysical Research Letters*, *52*(7), e2024GL113316. https://doi.org/10.1029/2024gl113316

Wolf, K., Bellouin, N., & Boucher, O. (2023). Long-term upper-troposphere climatology of potential contrail occurrence over the Paris area derived from radiosonde observations. *Atmospheric Chemistry and Physics*, *23*(1), 287–309. https://doi.org/10.5194/acp-23-287-2023

Zelinka, M. D., Klein, S. A., Qin, Y., & Myers, T. A. (2022). Evaluating climate models' cloud feedbacks against expert judgment. *Journal of Geophysical Research: Atmospheres*, *127*(2), e2021JD035198. https://doi.org/10.1029/2021jd035198

Zelinka, M. D., Myers, T. A., McCoy, D. T., Po-Chedley, S., Caldwell, P. M., Ceppi, P., et al. (2020). Causes of higher climate sensitivity in CMIP6 models. *Geophysical Research Letters*, *47*(1), e2019GL085782. https://doi.org/10.1029/2019gl085782

21698996, 2026, 8, Downloaded from https://agupubs.onlinelibrary.wiley.com/doi/10.1029/2025JD046235 by NICE, National Institute for Health and Care Excellence, Wiley Online Library on [30/04/2026]. See the Terms and Conditions (https://onlinelibrary.wiley.com/terms-and-conditions) on Wiley Online Library for rules of use; OA articles are governed by the applicable Creative Commons License